Plasma chemical aspects of an expanding thermal plasma in silane

Bastiaanssen, J.

Award date:
1996

Technische Universiteit Eindhoven
Faculteit der Technische Natuurkunde
Vakgroep Deeltjesfysica
Groep Plasma- en Atoomfysica

PLASMA CHEMICAL ASPECTS OF AN EXPANDING THERMAL PLASMA IN SILANE

Masters Thesis
Judith Bastiaanssen

VDF/NT 96-37 December 1996

Under supervision of:
Ir. R.J. Severens
Dr. M.C.M. van de Sanden
Prof. D.C. Schram

Summary

In the group Equilibrium and Transport in Plasmas, amorphous hydrogenated silicon films are deposited at high growth rates, by means of an $Ar/H_2/SiH_4$ expanding thermal plasma. The silane is dissociated to form, amongst others, SiH_2 and SiH_3 radicals, which determine the quality of the film. The surface reaction probabilities of the silane radicals have often been determined by other researchers, so that determination of this quantity for the particles in our plasma enables identification of the dominant radical. The plasma was analyzed by means of mass spectrometry, and from these measurements the silane depletion was determined, in order to gain further understanding of the chemical reactions in the plasma and the radicals formed in these reactions. SiH_3, which is expected to give rise to high quality films, appears to be the dominant radical at low plasma power and large hydrogen seed to the arc. Mass spectrometry analysis of an $Ar/D_2/SiH_4$ plasma confirms deuterated silane formation.

Table of Contents

1. Introduction

1.1 Amorphous Hydrogenated Silicon in Photovoltaic Cells

Solar cells, although not yet cost effective, are one of the most promising sources of energy to replace the waning fossil fuel resources; for this reason, a lot of research is being done on various production techniques of different kinds of solar cells. One of the types of photovoltaic cell being investigated is the amorphous hydrogenated silicon (a-Si:H) cell. Advantages of these cells are that they can be very thin and cheap to produce (they can be made on flexible substrates), and even semi-transparent. Usually the cells operate as follows: light enters the solar cell through the glass and passes through a transparent SnO layer and a boron-doped P-layer until it reaches a layer of intrinsic a-Si:H (The I-layer, see Figure 1.1). There, the incoming photons create an electron-hole pair, of which the hole is attracted by the P-layer whereas the electron is attracted by the phosphor-doped N-layer underneath the intrinsic layer. The back electrode usually consists of a layer of silver or aluminum.

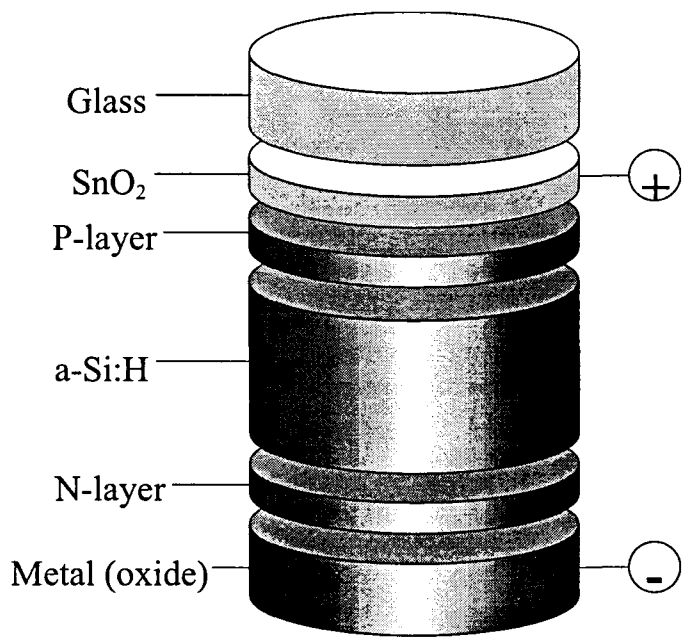

Figure 1.1: *The principle of a photovoltaic cell.*

In order to increase the efficiency of a photovoltaic cell an antireflective coating or rough interfaces between the different layers can be applied to minimize reflection[†]. As the intrinsic layer only absorbs light within a certain range of wavelengths, placing intrinsic layers that absorb different colors, each surrounded by P- and N-layers, on

[†] No antireflective coating is added to PV cells with a-Si:H I-layers, as reflection is minimized by the rough SnO layer.

top of each other, will increase the total light absorption. USSC has demonstrated an initial efficiency of 17 % (13 % stable) for such a triple bandgap cell.

It is the intrinsic a-Si:H layer with which we are concerned here. The properties of this film have to meet certain demands for use in a photovoltaic cell, some of which are listed in Table 1.1.

Table 1.1: *Desired properties for intrinsic a-Si:H [VER95].*

Property	Desired Value
Bandgap	1.6 eV
Refractive index (632 nm)	4.3
Microstructure	< 0.1
Photo conductivity	$> 10^{-5}$ $(\Omega cm)^{-1}$
Dark conductivity	$< 10^{-10}$ $(\Omega cm)^{-1}$
Photo sensitivity	$> 10^{5}$

The microstructure, which is defined as the ratio of the SiH_2-related 2100 cm^{-1} FTIR-peak over the SiH-related 2000 cm^{-1} peak, is a measure for the columnar structure and voids in the film; this should be as low as possible. The photoconductivity and dark conductivity determine the film's functioning in a solar cell. The photo sensitivity is equal to the ratio between the photo and dark conductivities. For more information, cf. [VER95].

There are various ways in which this film can be produced, amongst which the most common is Plasma Enhanced Chemical Vapor Deposition (PECVD). With this technique, a silane (SiH_4) glow discharge is formed between two parallel plates. PECVD succeeds in producing films of the desired quality and is used in the production of solar cells. Its main cutback is, however, the low growth rate of the films (upto approximately 1 nm/s). As the growth rate is one of the main cost-determining factors, a lot of research is concentrated on new techniques by means of which *device quality* a-Si:H films can be formed at a *higher growth rate.*

1.2 Expanding Thermal Plasma Deposition

A number of years ago, a new technique known as Expanding Thermal Plasma Deposition (ETP) was developed in the group Equilibrium and Transport in Plasmas, (ETP), at the Eindhoven University of Technology. This technique is based on an expanding plasma beam [SEV95a]. An argon/hydrogen plasma is created in a cascaded arc and then expands supersonically into a vacuum chamber. Just after the point of entry into the chamber, silane (SiH_4) is added to the beam. The silane is dissociated into radicals (SiH_x, with $0 \leq x < 4$) or ionized. The radicals and ions are carried further downstream by the plasma, until they reach a substrate where they can stick to form a film of a-Si:H. As the flux of radicals and ions is large due to a large SiH_4 flow and plasma power, the growth rate of these films is much higher than the growth rate using PECVD - growth rates of approximately 10 nm/s have given rise to good a-Si:H. Current research on ETP is aimed at producing device quality a-Si:H films at a high growth rate. Figure 1.2 shows the setup used in forming a-Si:H by

means of ETP [SEV95a]. As it is a remote plasma, the setup can be geometrically separated into three regions: the creation of the plasma, transport of the reactants, and the deposition itself.

Creation of the Plasma:
The plasma is created in the cascaded arc, at approximately 0.5 bar - the feed gas is argon with varying amounts of hydrogen admixed. In the cascaded arc, the plasma is generated by a DC discharge between three tungsten-thorium or tungsten-lanthanum cathodes and an anode plate. A stack of ten cooled and electrically insulated copper plates is placed between the cathode and the anode - the plasma is confined to the cylindrical space formed inside this stack.

Transport of the Reactants:
The plasma enters the vacuum chamber (where the typical pressure during operation is 0.2 mbar) through a nozzle and at first expands supersonically. After passing the shockfront the expansion into the vacuum chamber continues subsonically. Just after the nozzle, pure silane is added to the plasma beam; the plasma dissociates the silane into radicals and ions, which are carried downstream to the substrate holder. The plasma composition is analyzed by means of a Balzers quadrupole mass spectrometer.

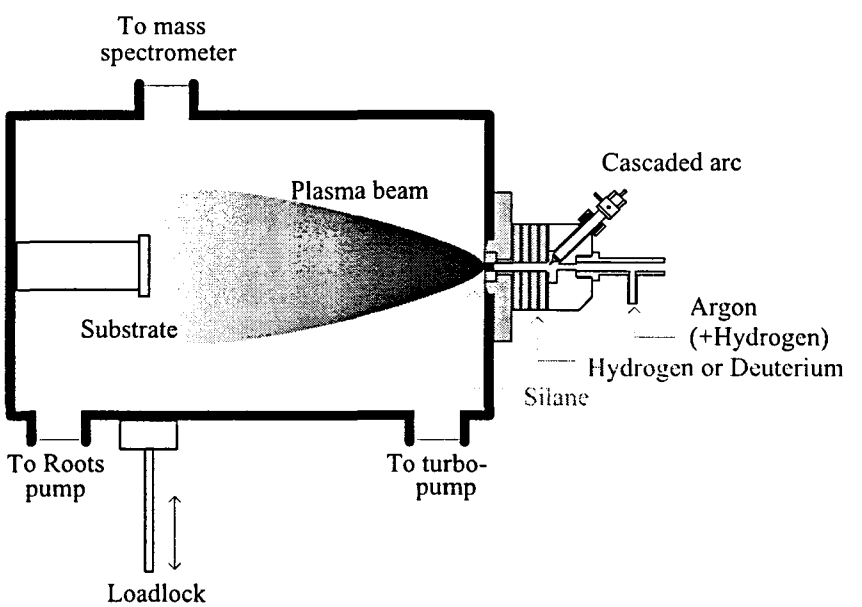

Figure 1.2: *The Expanding Thermal Plasma setup.*

Film Deposition:
In order to test our setup, a-Si:H films are usually deposited on c-Si substrates and on glass (Corning 7059). These c-Si substrates are clamped onto an aluminum or copper substrate holder which is moved into the vacuum chamber through a load lock. In the vacuum chamber, it is held in place on a yoke of which the temperature can be controlled. Heat transfer between the substrate holder and the yoke is optimized by means of helium backflow (Cf. [KES96] for details on helium backflow in a setup similar to this one). The temperature of the yoke is monitored with a thermocouple. The distance from the nozzle to the yoke is about 32 cm. Typical deposition times are from 30 seconds to two minutes, at a growth rate of 5 to 40 nm/s. Various settings

(temperatures, plasma current, and gas flows) influence the dissociation of silane and the condition of the film surface, and thereby the film quality.

As the film quality and growth rate are largely determined by the radical flux to the substrate and the composition of this radical flux, we would like to gain information on the conditions (plasma power, gas flows, substrate temperature, etc.) that give rise to 'good' radicals and preferably at high fluxes. But what is a 'good' radical?

1.3 Surface Reaction Probability

When a reactive particle impinges on a growing surface, it can reflect off the surface with probability r or react with the surface with probability β. Reaction with the surface consists of either sticking to form a layer (probability s) or reacting to form a gaseous product. Several researchers have examined the role played in deposition by the various silane radicals, as well as their surface reaction probabilities. The surface reaction probability of the SiH_3 radical (silyl) is generally found to be around 0.25, while those of the other radicals are approximately 0.7 for SiH_2 (silylene), 0.9 for SiH, and nearly unity for Si. The consensus appears to be that the radical that is principally responsible for deposition of high quality films is SiH_3 (cf. [GAL88], for example), because of its relatively low surface reaction probability and its high surface mobility. A consequence of the above is that if it is possible to measure the surface reaction probability of the radicals present during deposition, it is presumably possible to determine the type of radical present.

It is expected that the radical formed depends on the plasma conditions. Comparison of film qualities under different plasma conditions may lead to some insight into the conditions that lead to SiH_3. Previous depositions using the ETP setup have shown that varying the deposition conditions has the following effects (see also [SEV95b], [BRO96], and [KAA97]):

- Hydrogen flow: The refractive index of the film appears to increase with hydrogen flow, upto a maximum. The film growth rate is highest at zero hydrogen flow, decreases when hydrogen is added to the arc, but increases once again when the H_2 flow is increased further, see Figure 1.3.
- A higher substrate temperature (upto 500 °C) results in a somewhat lower film growth rate, but better film quality.
- A higher arc current also results in a higher film growth rate but lesser film quality.
- A higher pressure in the deposition chamber during deposition results in a higher film growth rate but a lesser overall film quality.

The best films produced so far have achieved device quality.

Apparently, the conditions for best film quality are an $Ar/H_2/SiH_4$ plasma with a low arc current, a high substrate temperature, and low pressure in the vacuum chamber. As the plasma is remote, the substrate temperature does not affect the radical production. It does, however, affect the film quality significantly, which suggests that the surface processes are of importance. As for the plasma conditions, if the SiH_3 radical is primarily responsible for deposition of high quality films, then the expectation would be that the arc, vessel, and flow conditions listed above result in SiH_3 production,

whereas no addition of H_2 to the arc, high arc current, and high pressure in the deposition chamber would result in production of the SiH_x ($x < 3$) radicals.

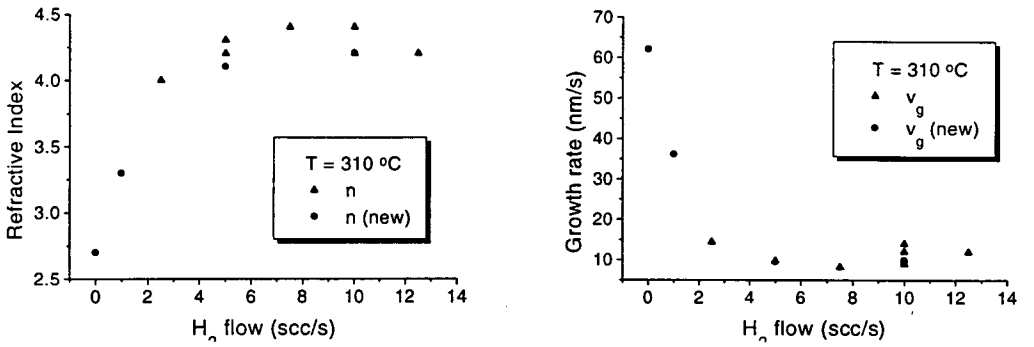

Figure 1.3: *Refractive index (a) and growth rate (b) versus hydrogen flow [KAA97].*

1.4 Radical Production in the Plasma

In the arc, argon is ionized to Ar^+, and hydrogen is dissociated and ionized. When silane is added to the plasma beam just after it enters the deposition chamber, it is dissociated into radicals and ions by the argon and hydrogen ions and radicals; these radicals can then stick to form the growing film. The amount of silane that is dissociated by the plasma is a measure for the (silane) radical flux to the substrate. In order to determine how much silane has been dissociated by the plasma, the partial pressures of silane with the plasma on and off can be measured by means of mass spectrometry. The mass spectrometer used cannot distinguish between SiH_4 and the SiH_x ($x<4$) radicals, which means that the radicals would still contribute to the silane signal measured, thus resulting in a value that is too high. However, these radicals have a certain probability of sticking to a surface, and they have ample opportunity to meet with the walls of the system several times before they meet the mass spectrometer. Therefore, it is assumed that the radicals do not make it to the mass spectrometer.

Silane depletion is defined as in equation (1.1):

$$\text{depletion} = \frac{P_{v,off}(SiH_4) - P_{v,on}(SiH_4)}{P_{v,off}(SiH_4)} \cdot 100\% \qquad (1.1)$$

It is determined by measuring the silane partial pressure in the deposition chamber with the plasma on $p_{on}(SiH_4)$ and off $p_{off}(SiH_4)$, by means of mass spectrometry. If the temperature of the sampled gas does not change when the plasma is turned on or off, the pressures can be replaced by densities.

Based on the reactions which are expected to occur in the plasma, a prediction can be made as to which conditions would be likely to result in SiH_3 production. Measurement of the silane depletion gives extra information on these reactions and is a measure for the radical flux.

1.5 Structure of this Thesis

In summary, we would like to know which deposition conditions lead to the production of the SiH_x ($x < 4$) radicals, and particularly to the production of SiH_3 as it is this radical that is believed to result in high quality films. Determination of the main radical present will be approached from two different perspectives: determination of the surface reaction probability and mass spectrometry on the deposition plasma. Chapter 2 deals with the plasma analysis. After describing the basic principles of mass spectrometry and calibration of the setup, mass spectrometry measurements on several plasmas are presented, as well as the resulting silane depletions. Conclusions on these measurements are also treated in this chapter. A method for determining the surface reaction coefficient of radicals is described in chapter 3, followed by measured values for β under different plasma conditions and conclusions. Chapter 4, finally, is directed at putting the results of chapters 2 and 3 together, resulting in overall conclusions and discussion.

2. Plasma Analysis

2.1 Introduction

The mass spectrometry results on the deposition plasmas are described in this chapter. The basic concepts of mass spectrometry, the experimental setup, and a description of typical mass spectra and their interpretation are included in chapter 2.2. However, correct interpretation of mass spectrometry results requires conversion to the partial gas pressures in the vacuum chamber, for which the system must be calibrated: this is treated in chapter 2.3. Subsequently, measurements on the residual gas in the deposition chamber are briefly presented in chapter 2.4. Results on argon/hydrogen/silane plasmas under various conditions, as well as an explanation of these results, follow in chapter 2.5. Depositions were also performed with deuterium instead of hydrogen - this is described in chapter 2.6. Finally, chapter 2.7 describes the measurements on the CF_4 plasma used to clean the deposition vessel after deposition, followed by a short summary in chapter 2.8.

2.2 Plasma Analysis by means of Mass Spectrometry

The basic principle of mass spectrometry is the following. First, molecules entering the mass spectrometer are ionized to ensure that they are sensitive to electric fields, by means of electron bombardment with electrons from a filament. The ions are then directed toward the mass filter and focused. Next, the ions are filtered in such a way that only *one mass* passes through to the detector.

The quadrupole mass filter consists of four hyperbolic electrodes with potentials such as shown in Figure 2.1. In practice, the hyperbolic electrodes are often replaced with rods of circular cross-section, with a specific radius that depends on the distance between the rods (see [DUC86]). The voltage consists of a DC voltage combined with an AC component:

$$\Phi_0 = U - V\cos\omega t \tag{2.1}$$

The equations of motion for a particle in such a potential are known as the Mathieu equations. From these, the conditions that lead to a stable trajectory are determined. In principle, for a given potential field, it is only the mass and ionic charge that determine whether an ion trajectory is stable or unstable. Thus, if the AC and DC voltage are set such that a certain mass-to-charge ratio *m/z* has a stable trajectory, it will pass through the quadrupole unhindered, whereas all other mass-to-charge ratios will collide either with the electrodes or with the outside wall.

The detector, a Channeltron (also known as a channel electron multiplier, see [WHI86]), consists of a curved hollow tube with contact leads at both ends and a semiconducting inner surface. Ions incident on one end (funnel shaped to collect them) generate secondary electrons which are carried along the tube by the

longitudinal field and generate yet more secondary electrons at each impact with the inner wall of the tube. The number of incoming particles determines the signal so that this signal is directly proportional to the partial pressure due to that mass.

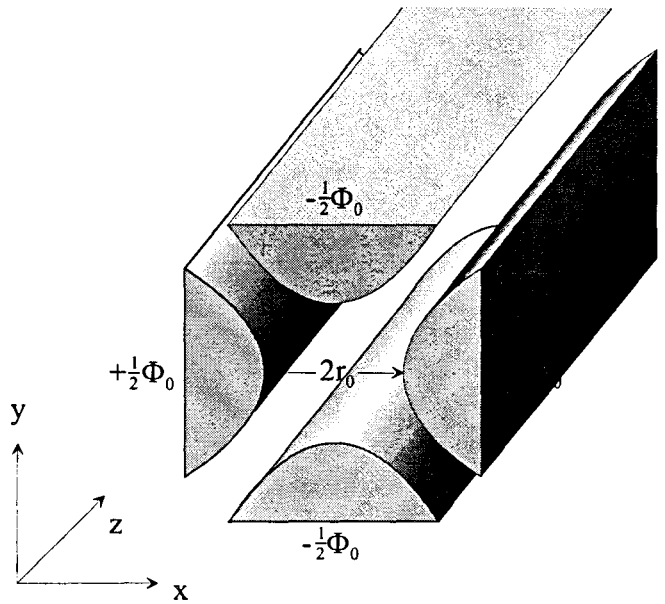

Figure 2.1: *The quadrupole.*

2.2.1 Experimental Setup

The mass spectrometer used to analyze the plasma is a Balzers Quadrupole, QMS 200 Prisma, which can measure mass ranges from m/z = 1 to 200. The detector is a Channeltron, with a detection limit of 10^{-14} A. As will be shown in section 2.3.3, this corresponds to an argon partial pressure of approximately 10^{-8} mbar in the deposition chamber. It is attached to the side of the vacuum vessel as shown in Figure 2.2. A Leybold 450 L/s Turbomolecular pump, in series with a rotational pump, pumps the deposition chamber between depositions, and brings the pressure down to approximately $3 \cdot 10^{-5}$ mbar. During depositions, however, the operating pressure in the vacuum chamber is normally around 0.2 mbar (due to an Edwards EH 2600 Rootsblower, a Balzers WKP 500 Rootsblower, and a rotational pump). The pressure in the deposition chamber is measured by means of barometers (for pressure ranges of 1000 to 1, and of 10 to 10^{-3} mbar) or with a Penning manometer for lower pressures. The pressure at the mass spectrometer must be maintained below 10^{-5} mbar, preferably around $2 \cdot 10^{-6}$ mbar. For this reason, a Balzers-Pfeiffer TMU 065 turbomolecular pump is attached to the mass spectrometry system as shown in Figure 2.2. To facilitate the pressure difference between the deposition chamber and the mass spectrometry vessel, a pinhole with a diameter of 100 μm is placed between these two - the turbopump extracts a small flow from the reaction chamber through the pinhole. The pressure in the mass spectrometer vessel is measured with a Balzers PKR250 Penning pressure meter.

The background Penning pressure in the mass spectrometer chamber is about $3 \cdot 10^{-8}$ mbar. To promote degassing of water that has been absorbed on the walls of the chamber, the chamber is baked out by means of a coil just above the turbopump (see

Figure 2.2). Just after turning on the mass spectrometer emission current, the penning pressure in the mass spectrometer vessel is seen to rise quickly to approximately $3 \cdot 10^{-7}$ mbar, due to degassing of the filament. The pressure slowly drops to its old level in about 20 minutes.

The QMS 200 has three measurement modes:

1. Scan analog
2. Scan bargraph: once the mass spectrometer is properly calibrated, spectra can be compared to the library spectra included in the software.
3. Multiple Ion Detection = MID: in which the concentration of a number of specified masses is measured as a function of time.

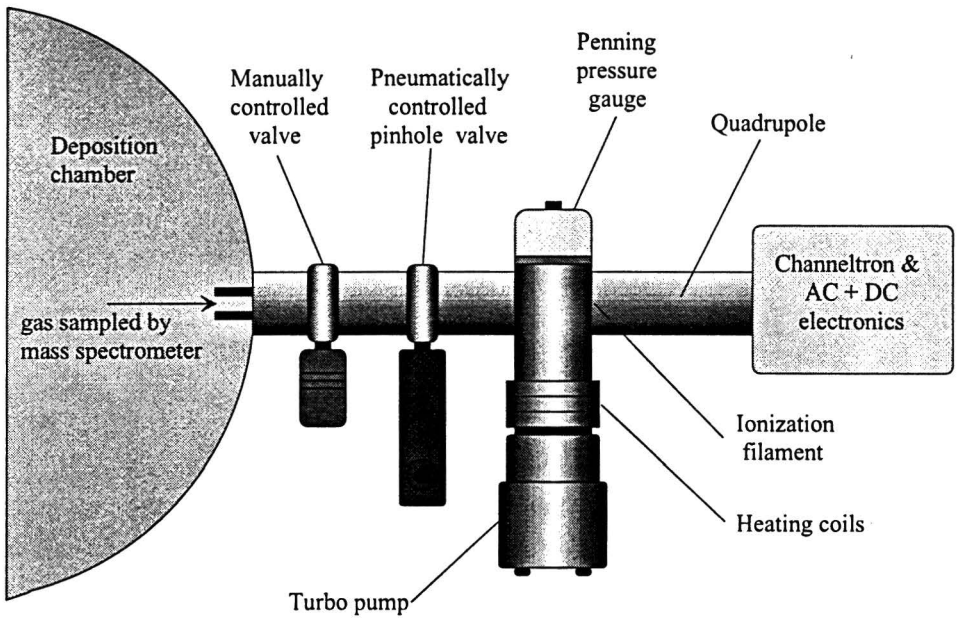

Figure 2.2: *The Balzers Quadrupole mass spectrometer, attached to the vacuum vessel.*

2.2.2 Fragmentation and Multiple Ionization of Molecules

In our measurements, the electron beam has an energy of 90 eV, which is high enough not only to ionize but also to fragment the sample molecules. A silane molecule (SiH_4), for example, may be broken down to any ion from SiH_3^+ down to Si^+ (the SiH_4^+ ion is unstable [LIB94]). The mass of the most common silane molecule is 32. Thus, m/z = 28 to 31 are all part of the fragmentation spectrum of silane. Masses with m/z = 32 and 33 are also seen in the fragmentation spectrum, due to Si isotopes of masses 29 and 30. Double ionization results in a peak at one half the value of the 'regular' peak, etc. The m/z values present in the fragmentation spectra of a number of the (in our case) most relevant gases are given in Table 2.1.

Problems arise when several gases with overlapping spectra are present. Typical examples of this in our case are silane and nitrogen, which both have peaks at m/z = 28, and silane and oxygen, which both have peaks at m/z = 32. The measured silane spectrum, for example, must be corrected for this effect by subtracting the measured

currents of *m/z* = 28 and 32 when no silane is present. Examples of the spectra of silane and disilane are given in Figure 2.3 and Figure 2.4

Table 2.1: *m/z values present in the fragmentation spectra of some of the most relevant gases.*

Gas	most important *m/z* values	main peak
SiH_4	28, 29, 30, 31, 32*, 33*	30
Ar	20†, 36*, 38*, 40	40
H_2	1, 2, 3	2
Air	7†, 8†, 14, 16, 28, 32, 40	28
H_2O	16, 17, 18	18
CO_2	12, 16, 22, 28, 44, 45	44
N_2	7†, 14, 28	28
O_2	8†, 16, 32	32
CF_4	19, 25, 31, 34, 50, 51, 69, 70	69
SiF_4	14, 19, 28, 33, 47, 66, 85, 86, 87, 104	85

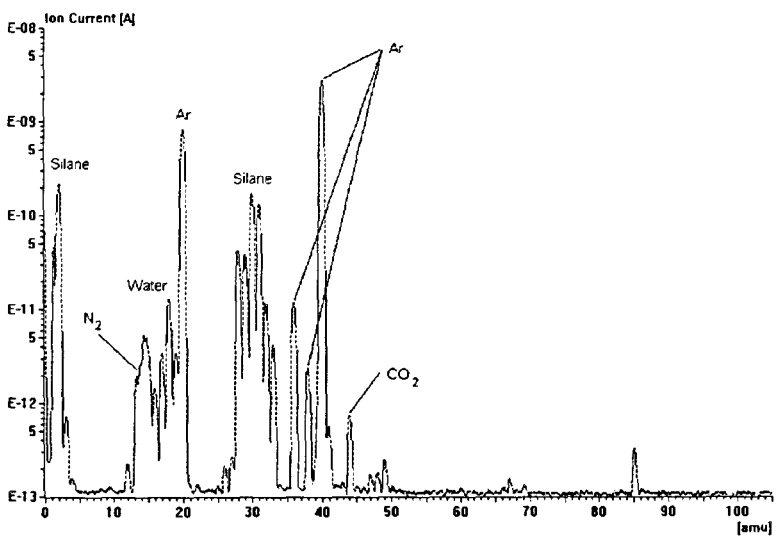

Figure 2.3: *Spectrum of silane.*

Note that *m/z* = 1, 2, and 3 are all part of the fragmentation spectrum of silane. The silane spectrum was measured when an argon flow of 55 scc/s and a silane flow of 4.5 scc/s were put into the vacuum chamber - there was no plasma. The disilane pressure was measured by filling the deposition chamber with pure disilane and then turning off the pumps. The argon signal which is still seen is due to gas still present from previous measurements.

* Due to an isotope.
† Due to double ionisation.

The mass spectrometer's response to pressure in the deposition chamber* varies with mass as $M^{-1/2}$. This correction must be made when analyzing the spectra: it particularly makes the peak at $m/z = 2$ look disproportionally large.

2.2.3 Measurement of Ions and Radicals

Being able to measure the ions and radicals in our plasma would offer a wealth of new information. However, ions cannot be detected as the setup is not equipped with ion focussing optics. Radicals cannot be detected separately either, as their *m/z* peaks cannot be distinguished from those of silane molecules†. As stated before, a silane molecule may be broken down to any ion from SiH_3^+ down to Si^+. Similarly, the SiH_3 radical, for example, may *also* be broken down to any ion from SiH_3^+ down to Si^+.

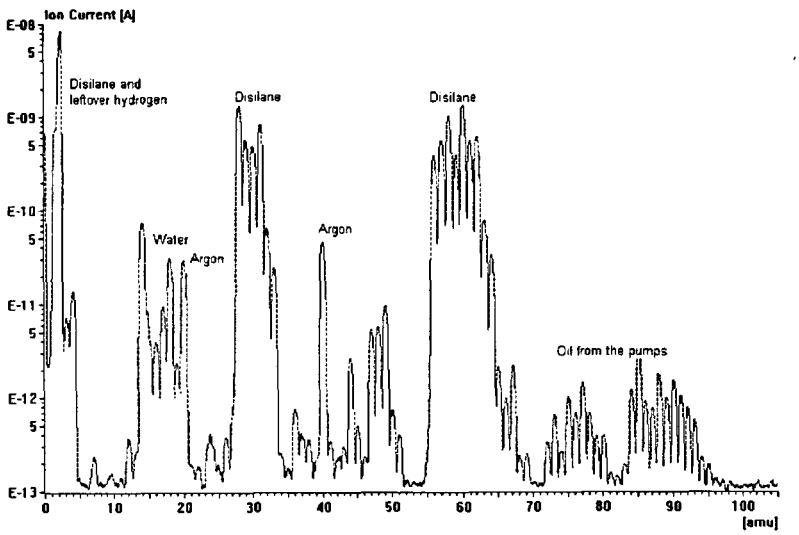

Figure 2.4: *Spectrum of disilane.*

2.3 Pressure Calibration of the Mass Spectrometer

2.3.1 Introduction

For correct interpretation, the mass spectrometer current must be converted to the relevant partial pressure in the reaction chamber. The partial pressure due to gas M, $P_v(M)$, in the vacuum chamber will give rise to a partial pressure $P_{MSM}(M)$ of gas M in the mass spectrometry vessel:

$$P_v(M) = \frac{S}{C(M)} P_{MSM}(M). \tag{2.2}$$

* Partly due to the mass spectrometer's sensitivity, which goes with 1/M [MOL95], and partly due to the conductance of the pipes, which goes with $M^{-1/2}$, as will be seen in section 2.3.2.

† There is a method by means of which SiH_4 and SiH_3, for example, *can* be distinguished: appearance potential mass spectrometry. This type of mass spectrometer makes use of an extremely finely energy tunable electron source and highlights the different threshold energies for ionization of the silane molecule and the various radicals. If, for example, the SiH_3^+ signal is measured as a function of the electron energy, this signal will increase when the SiH_3 ionization threshold is reached around 8 eV, and when the SiH_4 ionization threshold is reached, around 12 eV [ROB83], [ROB86], [KAE95].

Here, *C(M)* is the conductance of the system between the reaction chamber and the mass spectrometry chamber, and *S* is the turbopump's effective pumping speed, see Figure 2.5. The conductance, which is gas-dependent, can be calculated or determined from measurement. The effective pumping speed is also gas-dependent in the case of a turbomolecular pump: it depends entirely on the mass of the molecules being pumped. The pumping speed varies quite a bit for low masses, but becomes nearly constant for higher masses. Table 2.2 lists the pumping speeds of the Balzers-Pfeiffer TMU 065 turbopump as a function of the gas, as given in the specifications.

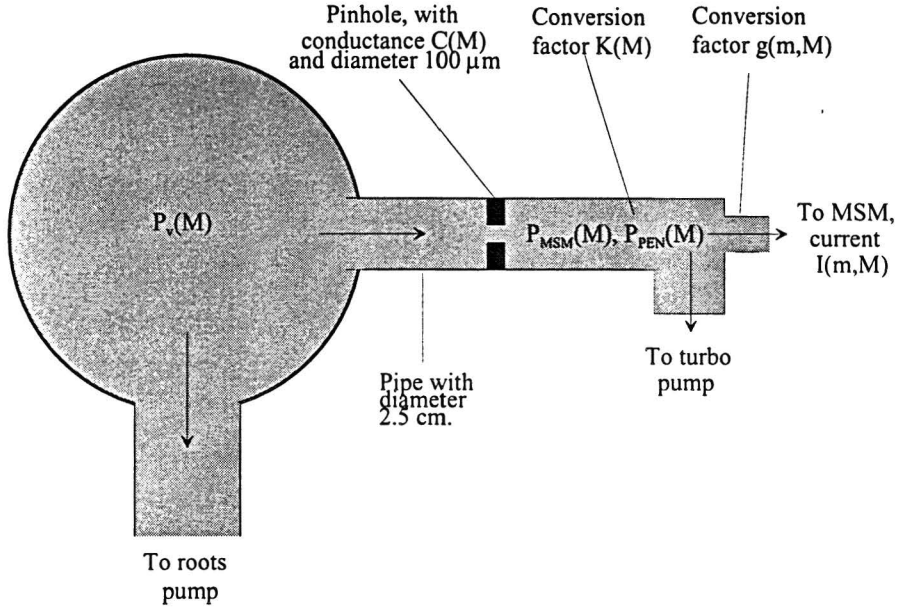

Figure 2.5: *Vacuum aspects of the mass spectrometer system.*

The measured current $I(\mu, M)$ at a certain $m/z = \mu$, due to gas M, is related to the pressure in the chamber [HAM94]:

$$P_v(M) = g(\mu, M) \cdot I(\mu, M) \cdot K(M) \cdot \frac{S}{C(M)}, \tag{2.3}$$

where $g(\mu, M)$ is a gas- and m/z-dependent conversion factor that represents the mass spectrometer's sensitivity to different masses, and $K(M)$ is a conversion factor from Penning pressure to absolute pressure, see Table 2.2. A Penning gauge measures pressure by ionizing gas atoms and measuring the resulting current. As the electrical conductivity of a gas depends on its density and on the gas itself, the Penning pressure has to be corrected for the mass of the gas [HAM94].

The current $I(\mu, M)$ is measured, the coefficient $K(M)$ is known for most gases, and the effective pumping speed of the gas is roughly known (for silane, it was estimated to be nearly the same as for nitrogen). The coefficient $g(\mu, M)$ must be determined by calibration. $C(M)$ can be determined either by calibration or calculation.

Note that the conversion factor *K(M)* between the Penning and the absolute pressures, the pumping speed *S*, and the mass spectrometer's sensitivity (expressed in $g(\mu, M)$) depend only on the gas being considered and therefore do not change when the plasma is turned on or off. If the flows through the system are molecular, the conductance *C(M)* is *independent* of pressure and therefore also only dependent on the mass; if the flows are laminar or intermediate, it *does* depend on the pressure in the vessel [MOL95].

Table 2.2: *Turbopump's effective pumping speed and the conversion factor from Penning to absolute pressure, for a number of gases.*

Gas	Pumping speed (L/s)	K
Nitrogen/Air	56	1.0
Helium	48	5.9
Hydrogen	36	2.4
Argon		0.8
Xenon		0.4
Silane		0.4*

For the depletion, this implies that:

$$\text{depletion} = \frac{P_{v,off}(\text{SiH}_4) - P_{v,on}(\text{SiH}_4)}{P_{v,off}(\text{SiH}_4)} \cdot 100\% = \frac{\frac{I_{off}(\text{SiH}_4)}{C_{off}(\text{SiH}_4)} - \frac{I_{on}(\text{SiH}_4)}{C_{on}(\text{SiH}_4)}}{\frac{I_{off}(\text{SiH}_4)}{C_{off}(\text{SiH}_4)}} \cdot 100\% . \quad (2.4)$$

If the system's conductance for silane does not change when the plasma is turned on or off (which is the case if the pressure does not change enough to change the type of flow, see Appendix A),

$$\text{depletion} = \frac{I_{off}(SiH_4) - I_{on}(SiH_4)}{I_{off}(SiH_4)} \cdot 100\% . \quad (2.5)$$

2.3.2 Calculation of the Pinhole Conductance

Compared to the pinhole, the resistance of the pipes leading from the vacuum chamber to the mass spectrometry vessel is negligible. Therefore, it suffices to calculate the conductance of the pinhole. In our vacuum system, the flow in the pipes just before the pinhole (on the high pressure side) is in the transition between laminar and molecular. In the pinhole and on the low-pressure side of it, however, the flow is definitely molecular (see Appendix A). For molecular flow through an aperture, the conductance of the aperture is equal to [SUU89] and [BER92]:

* Calculated in [HAM94].

$$C = \frac{1}{4}\sqrt{\frac{8kT}{\pi m}} \cdot A, \tag{2.6}$$

where m is the atomic mass and A is the area of the aperture. Inserting all values (and the mass of argon) results in a conductance of $7.8 \cdot 10^{-7}$ m^3/s. Conductance is gas-dependent: the conductance of the pinhole for other gases is roughly equal to

$$C_2 = C_1\sqrt{\frac{T_2 m_1}{T_1 m_2}}, \tag{2.7}$$

where m_1 and m_2 are the atomic masses of the different gases and the temperatures of the two gases are the same, in our case.

2.3.3 Calibration Results

The vacuum system was calibrated for argon, hydrogen, silane, and disilane. The argon calibration was performed as follows: with the roots pump working, a number of different argon flows from 20 to 80 scc/s were injected into the deposition chamber. The resulting pressure in the deposition chamber (P_v(Ar)), Penning pressure in the mass spectrometer vessel (P_{pen}(Ar)), and mass spectrometer current (I(40, Ar)) were measured for each flow. From these, using equation (2.3), the value for

$$\frac{g(40,\mathrm{Ar}) \cdot K(\mathrm{Ar})}{C(\mathrm{Ar})} = \frac{P_v(\mathrm{Ar})}{S \cdot I(40,\mathrm{Ar})} \tag{2.8}$$

was determined. For this, the pumping speed S of the turbopump must be known - it was estimated to be 60 L/s for argon.

Hydrogen calibration was performed differently, due to the turbopump's bad response to this light gas. With a standard argon flow, hydrogen flows from 0 to 20 scc/s were added to the reaction chamber. Once again, the constant in equation (2.8) could be determined; this time, however, a correction had to be made for argon. Using the measured argon current, the pressure in the vacuum chamber due to argon could be calculated using equation (2.3), and this was subtracted from the total pressure P_v to determine $P_v(H_2)$. Measurement was performed with $m/z = 2$.

Table 2.3: *Calibration results.*

Gas	g·K/C (mbar·s/A·m^3)
H_2	$5 \cdot 10^7$
Ar	$9.7 \cdot 10^8$
SiH_4	10^9
Si_2H_6	$3 \cdot 10^9$

Silane calibration was performed in the same manner as hydrogen calibration, once again correcting for the partial pressure of argon. Measurement was performed with

m/z = 30, and it was assumed that the pumping speed does not change with addition of silane.

Disilane calibration was performed differently. To avoid using up a large amount of this gas, we performed this measurement with an extremely small disilane flow and the roots pump turned off. As the pressure in the vessel increased, all measurable quantities were noted once again, and used to determine the constant in equation (2.8). Measurement was performed with the main disilane peak, at m/z = 60. Results of these calibrations are listed in Table 2.3. The units are such that multiplication by the measured current in A and the pumping speed of the mass spectrometer turbopump in m^3/s will yield the partial pressure in the vacuum chamber in mbar.

From these calibration results, the detection limit of the mass spectrometer can be determined. In the case of argon, its detection limit of 10^{-14} A corresponds to a partial pressure in the deposition chamber of $6 \cdot 10^{-7}$ mbar. For hydrogen and disilane the detection limits are pressures of $2 \cdot 10^{-8}$ and $2 \cdot 10^{-6}$ mbar.

2.4 Residual Gas Analysis

A scan of all masses present in the vacuum chamber after baking out with an argon plasma and several days of turbo-pumping is shown in Figure 2.6. This scan was measured with the pinhole removed from the system so that the mass spectrometry vessel was directly connected to the reaction chamber via the pipes. The pressure in the vacuum chamber was $1.4 \cdot 10^{-5}$ mbar, which is so low that the pressure in the mass spectrometry vessel remained below its maximum value of $1 \cdot 10^{-5}$ mbar without the pinhole (due to the resistance of the pipe leading to the mass spectrometer - when the pinhole is in place, the resistance of the pipe is negligible compared to that of the pinhole). The main signal at m/z = 28 is due to nitrogen, from the air, accompanied by peaks at 14 and 7. Other important peaks are due to argon (m/z = 40 and 20), oxygen (at m/z = 32 and 16), water (around m/z = 18), CO_2 (44), and hydrogen (2).

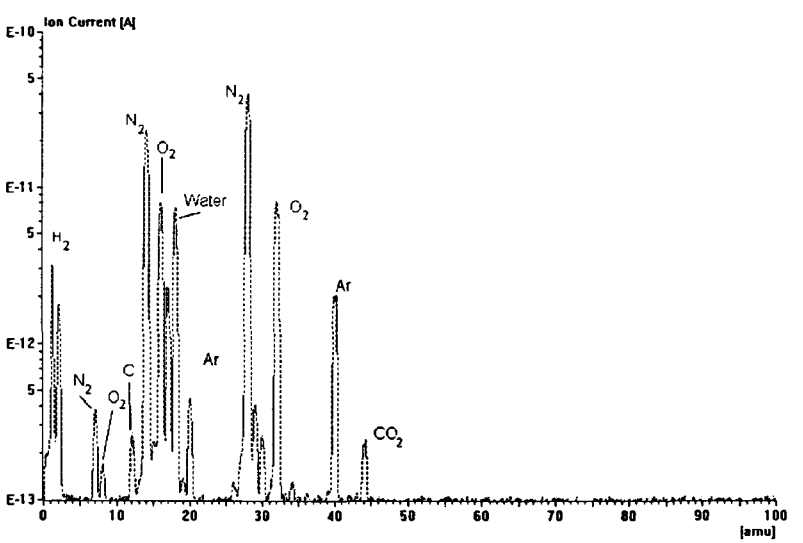

Figure 2.6: *Gases present in the vacuum chamber when under low pressure.*

2.5 Mass Spectrometry Results on Deposition Plasmas with Hydrogen

2.5.1 A Typical Deposition Plasma

During deposition, the usual measurement mode is MID - multiple ion detection versus time. Because of the trade-off between the mass spectrometer time response and the number of masses measured, a selection was made of the masses to be measured. The *m/z* values usually measured are:

Table 2.4: *Values of m/z usually tracked versus time, during deposition.*

m/z	Source
1, 2, 3	hydrogen
16, 18	oxygen and water contamination
28 - 33	silane
40	argon
60	disilane
84	trisilane

A typical MID measurement performed during deposition is shown in Figure 2.7. About 140 seconds after the start of the measurement, the valve connecting the mass spectrometry vessel to the deposition vessel was opened. An argon flow was present in the deposition chamber, resulting in a large increase in the value of $m/z = 40$. After 165 seconds, the plasma was turned on. This results in a peak in the signal of all gases, probably due to a shock passing through the chamber. Note also that the $m/z = 40$ signal after the plasma is turned on is the same as before: this means that the temperature of the gas that is sampled does not change significantly, and that the conductance of the system remains unchanged. Next, after about 175 seconds, hydrogen was added to the arc - this is easily recognizable by the increase in $m/z = 2$. Then, after 220 seconds, silane is added. This results in an increase in the $m/z = 30$ peak, as well as the appearance of $m/z = 60$: disilane is being formed. Note that $m/z = 2$ increases as well. This is caused by two effects: first of all, $m/z = 2$ is a standard peak in the silane fragmentation spectrum so that addition of SiH_4 automatically increases the $m/z = 2$ signal. Secondly, the plasma dissociates silane into, amongst other products, H_2, which again increases the peak at $m/z = 2$. Thirdly, atomic hydrogen may be formed when silane is dissociated. This H may then form H_2 when it associates with H atoms at the walls, and desorb back into the vessel. When, about 80 seconds later, the plasma is turned off, several effects are noted. First of all, a small peak arises in all signals, once again probably due to non-stationary effects. In the second place, the silane signal increases, indicating that silane is no longer being broken down by the plasma. The silane depletion is determined by comparing the value that $m/z = 30$ now climbs to to the value with the plasma on. This is accompanied by a decrease in the hydrogen signal, as hydrogen is no longer being extracted from silane in the plasma. This indicates that more H_2 is formed in the

plasma dissociation of silane than in the mass spectrometer's fragmentation of silane as the contribution due to fragmentation should rise with the *m/z* = 30 current. As most of the hydrogen in the silane molecule remains bonded to the silicon even when silane is fragmented (the largest peak at *m/z* = 30 is due to SiH_2^+), this is to be expected. Finally, the disilane signal disappears: apparently, disilane is only present in the chamber when silane is present and the plasma is on. After about 325 seconds, the silane flow was turned off, and finally the hydrogen and argon flows were also turned off.

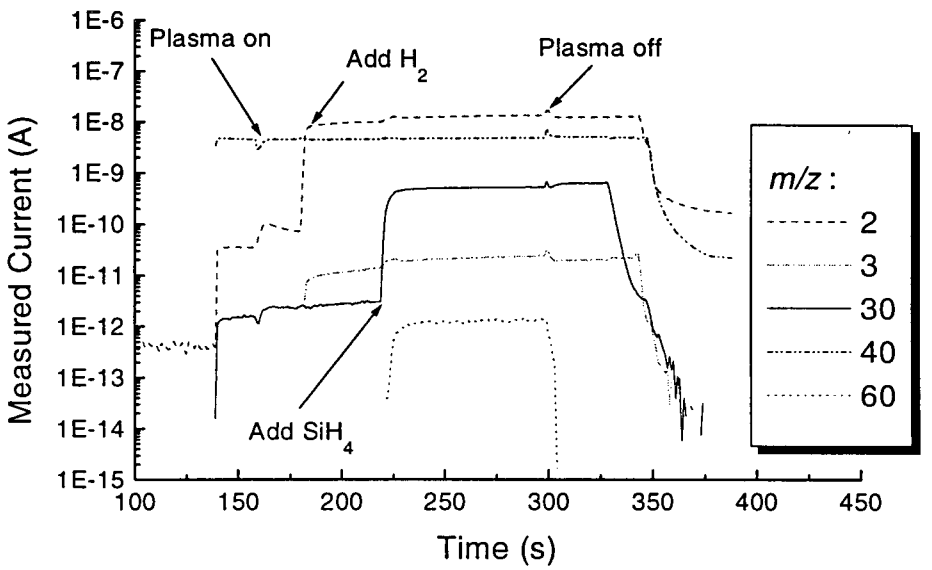

Figure 2.7: *Time-dependent measurement during deposition (RS204).*

When the plasma is turned off, the disilane signal disappears quickly, within a few seconds. The silane signal also appears to decrease at a fairly constant rate when the silane flow is turned off. The hydrogen, and argon signals, however, drop rapidly at first, after their respective flows are turned off, and then continue decreasing at a lower rate; it appears that removal of gases in the chamber is governed by two different time constants. In the case of hydrogen, this observation could be explained by hydrogen lagging in the mass spectrometry vessel, as the mass spectrometer's turbopump has a low pumping capacity for hydrogen.

2.5.2 Silane Depletion

In Figure 2.8, the arc current was varied, while the argon and hydrogen flows were kept at standard conditions (flows of 55 scc/s and 10 scc/s, respectively). The silane flow was 20 scc/s*. It is the depletion of *m/z* = 30 which is shown - the depletion curves for the other masses look nearly identical. Disilane was formed during this measurement, meaning that corrections should be made for the disilane signal at *m/z* = 30. However, in all of our measurements, the partial pressure in the deposition

* The standard silane flow was 10 scc/s. However, recalibration of the silane flowmeter between the measurement in Fig. 2.9 and that in Fig. 2.10 indicated that the 'old' silane flow corresponds to a 'new' silane flow of 20 scc/s.

chamber due to disilane, calculated from $m/z = 60$, is approximately 1% of the partial pressure due to silane (calculated from $m/z = 30$). Furthermore, as can be seen from Figure 2.4, the disilane peak height at $m/z = 30$ is approximately 30% of the maximum peak height at $m/z = 60$. Therefore, the disilane contribution to the peak at $m/z = 30$ may be neglected.

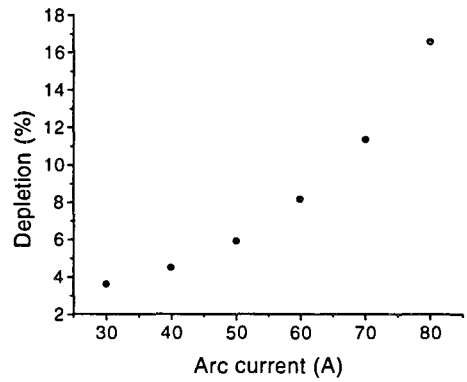

Figure 2.8: *Silane depletion versus arc current (DEPL011).*

Apparently, silane depletion increases for higher arc current. In the arc, argon is ionized by means of electron collision - this requires 15.8 eV. As the arc current is increased, more electrons are released, resulting in more argon ions and therefore a higher silane depletion.

Figure 2.9 (a) shows the silane depletion versus the silane flow. However, plotting the silane depletion versus the silane flow is not relevant, as the silane depletion is a *relative* breakdown of silane. Therefore, Figure 2.9 (b) is included, which shows the equivalent radical flow: that is, the absolute breakdown of silane, the current measured with the plasma off minus the current measured with the plasma on. The other conditions are standard: the argon and hydrogen flows were 55 and 10 scc/s, respectively, and the arc current was 45 A.

Silane depletion decreases with silane flow. However, the absolute breakdown of silane increases with silane flow, upto a maximum. This is explained as follows: when little silane is present, ions and radicals are in excess. In that case, addition of SiH_4 will result in further dissociation of SiH_4 - the depletion is limited by the amount of silane present. When, however, silane is in excess, addition of even more will *not* result in a further dissociation of silane as the reactions are limited by the number of ions, metastables, and radicals present.

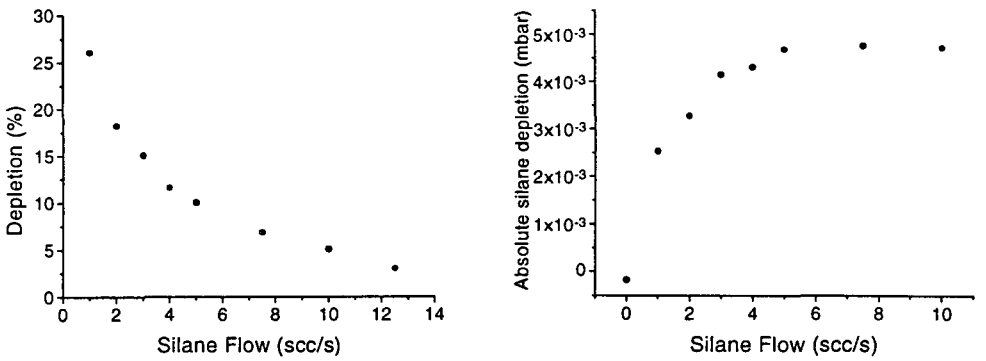

Figure 2.9: *Silane depletion and absolute silane breakdown, versus silane flow (DEPL012).*

Silane depletion with varying hydrogen flow was measured at two different silane flows. Figure 2.10 (a) shows the depletion at a silane flow of 20 scc/s, (b) shows the depletion at a silane flow of 10 scc/s, and (c) shows the depletion at a silane flow of 2 scc/s. Note the overall resemblance to the curve depicting the growth rate versus the hydrogen flow in Figure 1.3! This indicates that silane depletion is, in fact, a good measure for the radical flux to the substrate, and therefore for the growth rate of the film.

2.5.3 Discussion on Silane Depletion Results

Figure 2.10 shows the difference between silane breakdown by argon ions or metastables and by atomic hydrogen. When no hydrogen is added to the arc, silane is depleted entirely by argon ions (see Appendix B for reaction constants) [KUS88], [KUS92], [PER96]:

$$Ar^+ + SiH_4 \rightarrow SiH_3^+ + H + Ar, \tag{2.9}$$

immediately followed by

$$SiH_3^+ + e^- \rightarrow SiH_2 + H. \tag{2.10}$$

In our setup, silane is not dissociated by means of electron collision. This requires an electron energy of 8 eV [ROB86], whereas the electron temperature in the plasma beam, where silane is added, has dropped to approximately 0.2 eV. As shown in Figure 2.8, silane depletion increases for higher arc current, which results in more argon ions. When hydrogen is added to the arc, it is dissociated (4.4 eV) and can also be ionized (13.6 eV) [GRI94]. In that case, silane may also be dissociated by means of hydrogen ions, as shown in reaction (2.11), again followed by (2.10)

$$H^+ + SiH_4 \rightarrow SiH_3^+ + H_2, \tag{2.11}$$

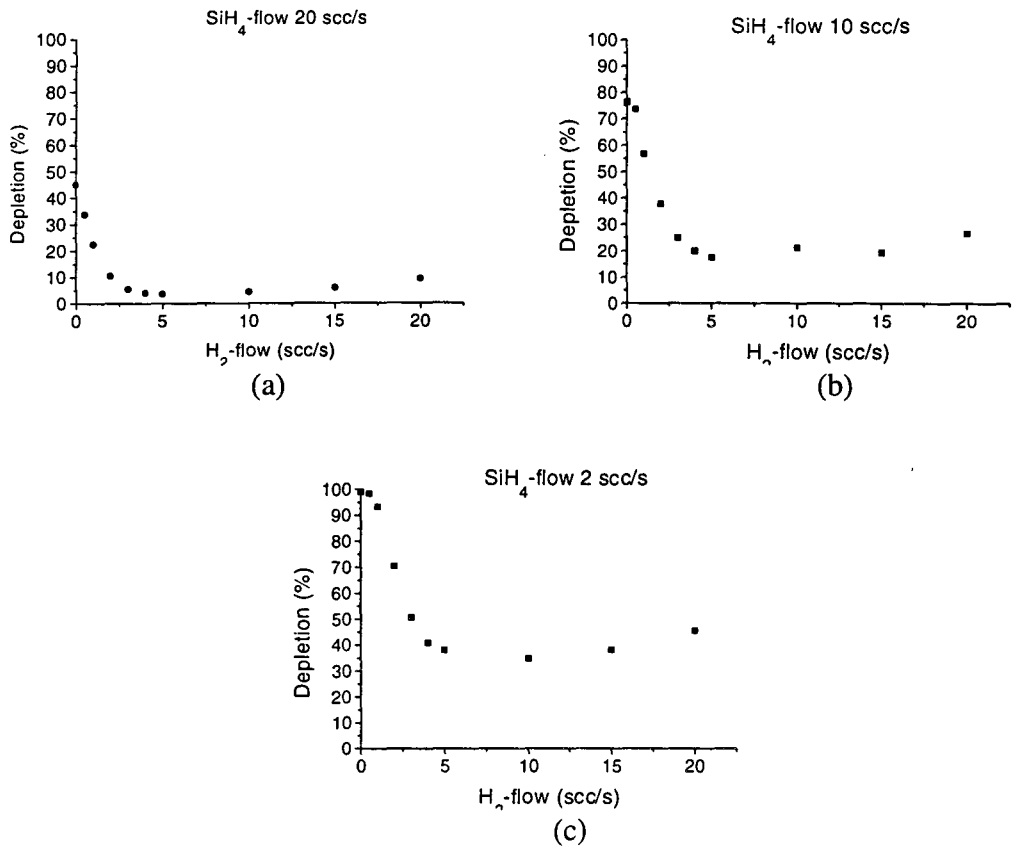

Figure 2.10: *Silane depletion versus hydrogen flow, at silane flows of 20 (a), 10 (b), and 2 (c) scc/s (DEPL10/13/14).*

Thus, silane dissociation by means of ions results in SiH_2. According to Kushner, the reaction of argon metastables with silane results in production of SiH_x ($x \leq 3$) radicals. The reaction constant for the production of SiH_2 is largest, at $4.6 \cdot 10^{-10}$ cm^3/s. Next is the reaction constant for the production of SiH_3: $1.4 \cdot 10^{-10}$ cm^3/s. The reaction constants for the production of the SiH and Si radicals by means of metastables are one and two orders lower, at $2.4 \cdot 10^{-11}$ cm^3/s and $1.8 \cdot 10^{-12}$ cm^3/s, respectively [KUS88] and [KUS92].

The dominant effect when hydrogen is added to the arc is not an increase in the silane depletion due to the formation of H^+, but the quenching of both argon and hydrogen ions by means of reactions (2.12) through (2.14), resulting in a rapid decrease in the silane depletion. Argon ions are quenched by means of the following reactions [KUS88]:

$$Ar^+ + H_2 \rightarrow ArH^+ + H, \qquad (2.12)$$

followed by:

$$ArH^+ + e^- \rightarrow Ar + H. \quad (2.13)$$

Hydrogen ions are quenched by means of charge exchange:

$$H^+ + H_2 \rightarrow H_2^+ + H. \quad (2.14)$$

The ionization degree of the expanding plasma is known to decrease when hydrogen is added to the arc [MEU96]. Then, as more hydrogen is added, silane depletion by means of reaction (2.15) takes over, and it increases once again [KUS87], [KUS88], [PER96], [MOR86]. As Figure 2.10 indicates, silane depletion by means of argon ions is far more efficient than by means of atomic hydrogen.

$$H + SiH_4 \rightarrow SiH_3 + H_2. \quad (2.15)$$

As silane dissociation by means of ions results in SiH_2, it appears that a plasma under these conditions must yield radicals with a high surface reaction probability of around 0.7. Silane dissociation by means of hydrogen, however, results in the desired SiH_3. Therefore, the expectation is that radicals formed when a considerable amount of H_2 is added to the arc will have a surface reaction probability of approximately 0.3.

Influence of Recirculation:
Atomic hydrogen that reaches the substrate holder without reacting is carried to the walls of the vessel, where it recombines with adsorbed atomic hydrogen to form molecular hydrogen. The time needed for particles to be carried from the nozzle of the plasma to the substrate holder is estimated to be around 0.3 ms. However, the residence time in the vessel is approximately 300 ms (the volume of the vessel is 170 L and the Roots pump has a pumping capacity of 700 L/s). In other words, particles spend more time in the background gas than in the plasma beam, implying that there must be recirculation. Thus, molecular hydrogen recirculating through the vessel may possibly re-enter the plasma beam and take part in any reactions taking place there. Proof of recirculation is given by Meulenbroeks et. al. [MEU96]. They measured the downstream electron density in the plasma beam, when H_2 was added to the arc or injected directly into the vacuum vessel. The results turned out to be the same, indicating that the hydrogen injected into the vessel must recirculate and even re-enter the plasma beam. More recent measurements, by Gielen et. al. [GIE96], have shown that at most 30% of the hydrogen recirculating in the vessel re-enters the plasma beam.

However, a point that can be made from the measurements in this chapter is that molecular hydrogen recirculating in the vessel does not have a lot of influence on the depletion of silane, and therefore is not responsible for the quenching of the argon ions. This can be seen as follows: when no hydrogen is added to the arc, and the depletion is high (80 %), this means that a lot of hydrogen is produced in the breakdown of silane (a rough estimate: 80 % of the silane flow of 10 scc/s is broken down, so that a hydrogen 'flow' of 8 scc/s would be formed. However, every silane molecule, if completely dissociated, yields two hydrogen molecules, thus resulting in a hydrogen 'flow' of 16 scc/s). This hydrogen recirculates around the vessel and can re-enter the plasma beam. If it were, however, to quench the argon ions, this would automatically result in a dramatic decrease in the depletion, as the silane depletion at a

hydrogen flow of 16 scc/s is only about 20 %. It is known, however, that H_2 *does* re-enter the plasma beam [MEU96]. These observations are consistent if all reactions take place near the shock (close to where silane is injected into the plasma beam from a ring surrounding the plasma) and if the recirculating H_2 *cannot* enter the plasma beam that close to the shock. This is possible if SiH_4 is supersonically injected into the plasma beam, so that it can enter at the shock, whereas recirculating hydrogen cannot enter near the shock and is expelled from the beam by the rapidly expanding gases.

2.5.4 On the Formation of Disilane

The mass spectrometry measurements on plasmas under the different conditions stated in section 2.5.2 showed the following: disilane production decreases with arc current, increases with silane flow, and increases with hydrogen flow. There appears to be a general correlation with the silane partial pressure, as shown in Figure 2.11. It turns out that in all cases the disilane partial pressure of the order of 1% of the silane partial pressure.

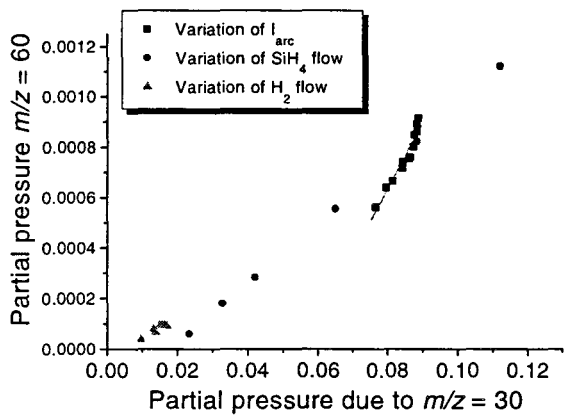

Figure 2.11: *The disilane partial pressure in the deposition chamber, versus the silane partial pressure.*

Disilane and trisilane (which we, however, barely measure and have not calibrated for) are formed in the following reactions [KUS88], [PER96], [GRI94]:

$$SiH_4 + SiH_2 \rightarrow Si_2H_6^*, \tag{2.16}$$

$$SiH_4 + Si_2H_6^* \rightarrow Si_2H_6, \tag{2.17}$$

$$SiH_2 + Si_2H_6 \rightarrow Si_3H_8. \tag{2.18}$$

Figure 2.11 would indicate that it is the density of SiH_4 and not that of SiH_2 which primarily limits the amount of Si_2H_6 formed.

At low hydrogen seed, the silane depletion is high and SiH_2 is probably the radical formed; this means that little silane is left to react in equation (2.16), and it is the limiting factor. In that case, addition of silane would clearly lead to an increase in the amount of disilane formed. When a large hydrogen flow is added to the arc, the dependence on silane flow is not as obvious, as the silane depletion is low and it is

primarily the SiH_3 radical which is formed. A possible explanation is that SiH_2 is now formed from SiH_3 by means of interaction with hydrogen:

$$SiH_3 + H \rightarrow SiH_2 + H_2 \tag{2.19}$$

This would, however, not explain the dependence of the disilane production on the silane present, as there will always be less SiH_3 than SiH_4, and even less SiH_2. Therefore, this is not a likely explanation.

A third possibility would be the formation of disilane from the recombination of two SiH_3 radicals on the surface. If silane is dissociated into SiH_3, then addition of silane will result in the formation of more SiH_3, which could then result in more disilane.

From Figure 2.11, it is difficult to judge whether the dependency is linear or quadratic - both fit the ponts fairly well. However, a quadratic dependency is to be expected (to first order approximation), as disilane production depends on the silane density but also on the SiH_2/SiH_3 radical density, which in turn depends once more on the silane density.

2.6 Mass Spectrometry Results on Deposition with Deuterium

Depositions were also performed using deuterium instead of hydrogen. Their chemical properties are identical but ERDA and FTIR are able to distinguish between the two sources of hydrogen in the film: that which was added to the arc and that which comes from the silane molecule.

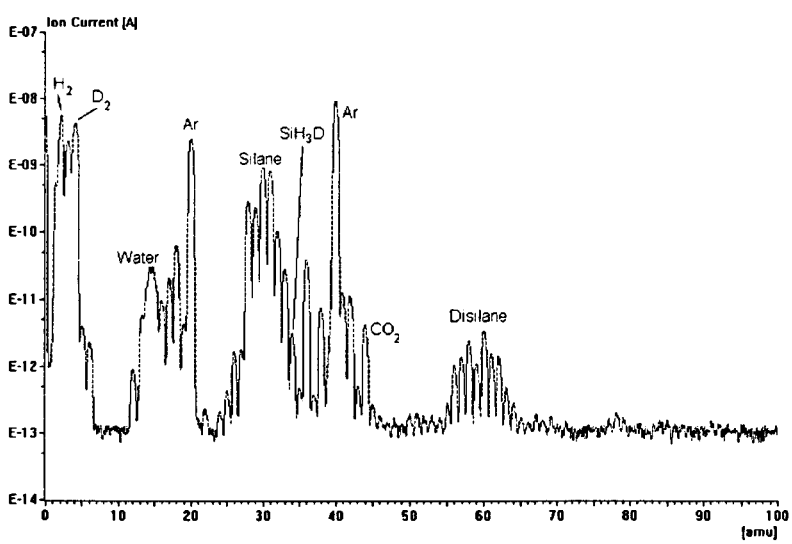

Figure 2.12: *Scan of an $Ar/D_2/SiH_4$ plasma spectrum (DEUT02).*

Figure 2.12 shows an analog scan of an $Ar/D_2/SiH_4$ plasma. Note the presence of *m/z* = 4 (D_2^+), 5, 6, and 34. Figure 2.13 shows a time-dependent measurement of an $Ar/D_2/SiH_4$ plasma, in which the D_2 flow is once again varied as noted in the figure. The argon and silane flows were 55 and 20 scc/s, respectively, and the arc current was equal to 45 A. The (unusual) *m/z* values that are measured are clarified as follows:

- *m/z* = 2 is formed in the dissociation of silane (H_2, which is ionized to H_2^+ in the mass spectrometer), and is also part of the silane fragmentation spectrum. It scales with the depletion.
- *m/z* = 3 comes from HD (HD^+). When the plasma is on, the hydrogen comes from silane dissociation in the plasma. When the plasma is off, however, hydrogen is only formed in the fragmentation of silane in the mass spectrometry vessel, and the signal is much lower.
- *m/z* = 4 is to D_2 (ionized to D_2^+ in the mass spectrometer).
- *m/z* = 5 is due to D_2H^+, formed in the mass spectrometer.
- *m/z* = 6 is due to D_3^+.
- *m/z* = 34 is due to SiH_3D, which is ionized to form SiH_2D^+ in the mass spectrometer. Isotope ^{30}Si then yields *m/z* = 34. Its signal is approximately 4% of that of silane. Other deuterated silane combinations could also give rise to a signal at this *m/z* value, but their contributions are slight. See Appendix H.

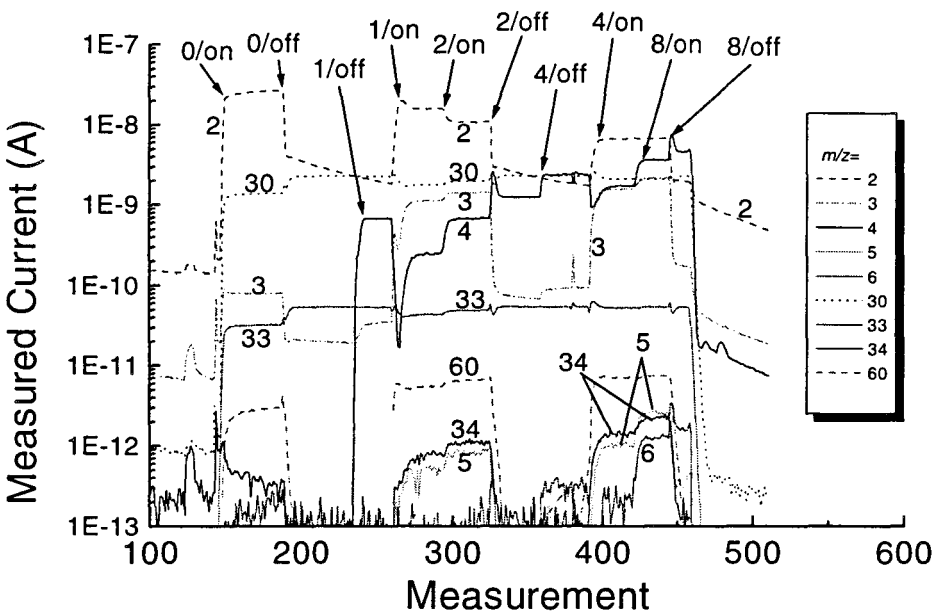

Figure 2.13: *Measurement on an Ar/D_2/SiH_4 plasma, with variation of D_2 flow as indicated in the figure (DEUT09).*

Deuterated silane is most probably formed when radicals interact with the walls of the system. As the dominant deuterated silane measured is SiH_3D, this suggests that SiH_3 was formed when silane was dissociated in the plasma; upon impact with the wall, it recombined to form SiH_3D. The detection of a higher SiH_3D density as the deuterium flow increases is consistent with the theory that SiH_3 is the dominant radical formed when silane is broken down by hydrogen (or deuterium). Additionally, the fact that SiH_2D_2 is not seen conforms with the theory that SiH_2 radicals do not recombine when incident on a surface, but that they always stick.

Finally, Figure 2.14 shows the silane depletion as a function of the deuterium flow - this was taken from the measurement shown in Figure 2.13. The argon flow was 55

scc/s, the silane flow 20 scc/s, and the arc current 45 A. The trend appears to be much the same as the curve for the silane depletion versus the hydrogen flow (Figure 2.10) except that it appears to lie at an altogether higher value. The lower depletion of masses 32 and 33 (i.e. less breakdown by the plasma or creation when the plasma is on) could be explained by the formation of deuterated silane when the plasma is on, which would result in peaks at those masses. Thus, it appears that silane depletion in an argon plasma with deuterium is more efficient than in an argon plasma with hydrogen. A possible explanation could be that, due to its higher mass, deuterium does not diffuse out of the plasma beam as well as hydrogen does, thereby resulting in a higher deuterium density.

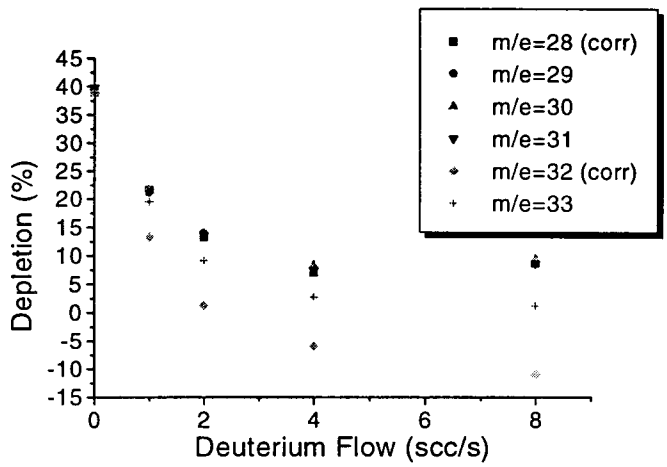

Figure 2.14: *Silane depletion as a function of deuterium flow.*

2.7 CF_4 Cleaning Results

In order to clean the silicon oxide deposits off the deposition vessel walls, vacuum cleaning is a possibility. A far more attractive option, however, is the use of a tetrafluoromethane, or CF_4, plasma. When CF_4 is added to the argon plasma, it is dissociated. The carbon binds to oxygen also injected into the plasma and forms CO and/or CO_2, leaving the fluorine to bind to silicon on the vessel walls to form SiF_4. These gases are all pumped out of the system, resulting in a clean deposition vessel. In order to monitor the effects of the gases and the arc current on the products, a number of mass spectrometry measurements were performed under various conditions. First, a scan of an $Ar/O_2/CF_4$ plasma is given in Figure 2.15. This scan was made under the 'standard' conditions, that is, argon, oxygen, and CF_4 flows of 53, 5, and 8 scc/s respectively (note, however, that the flowmeters are not calibrated for oxygen and CF_4) and an arc current of 75 A.

Variation in a number of masses, with varying plasma current, is shown in Figure 2.16. As the arc current is increased in steps, the SiF_4 production increases (m/z = 28) which means that the vessel is being cleaned more rapidly. The oxygen peak at m/z = 32 drops slightly, indicating that more oxygen is consumed at a higher arc current. Finally, the peak at m/z = 69, due to CF_4, decreases with increasing current, which is consistent with a higher reactivity and faster cleaning of the vessel.

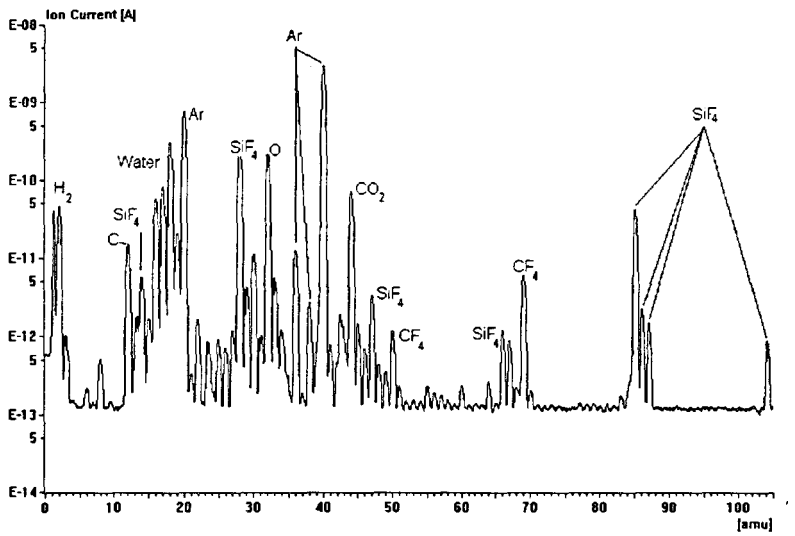

Figure 2.15: *An analog scan of an $Ar/O_2/CF_4$ plasma.*

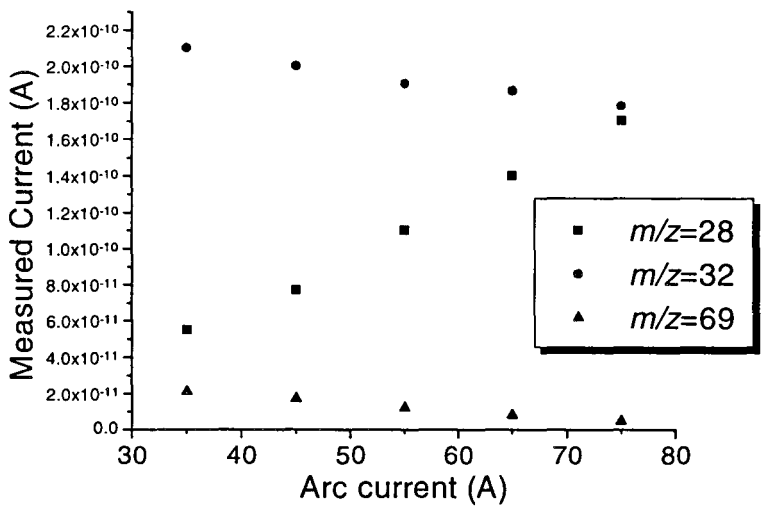

Figure 2.16: *Measurement on an $Ar/O_2/CF_4$ plasma, with variation of the plasma current.*

Next, the effect of oxygen flow is shown in Figure 2.17. Note that SiF_4 is only released, and CF_4 consumed, when oxygen is added, but that they are not dependent on the oxygen flow. This indicates that oxygen is already in excess at a flow of 5 scc/s.

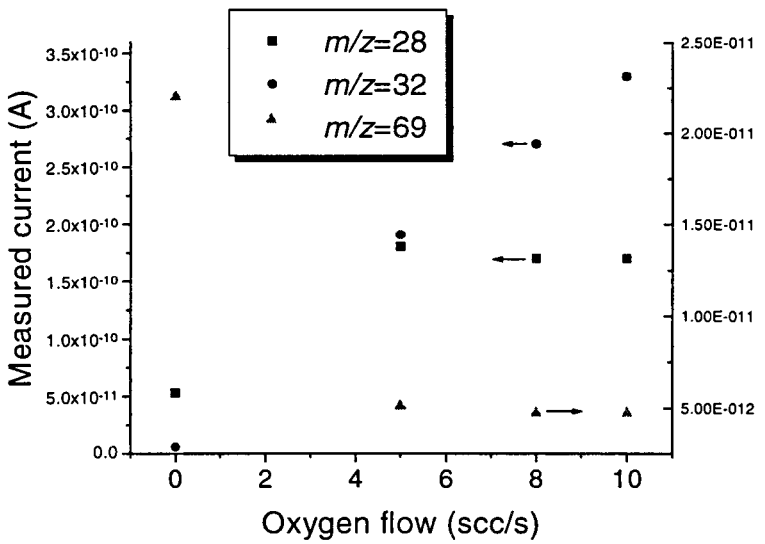

Figure 2.17: *Measurement on an $Ar/O_2/CF_4$ plasma, with variation of the oxygen flow.*

Finally, the effect of varying the CF_4 flow is monitored - see Figure 2.18. The peak at m/z = 32 does not vary, indicating that oxygen is in excess. This time, however, both CF_4 and SiF_4 increase with CF_4 flow: as more CF_4 is added, more of it is used to form SiF_4.

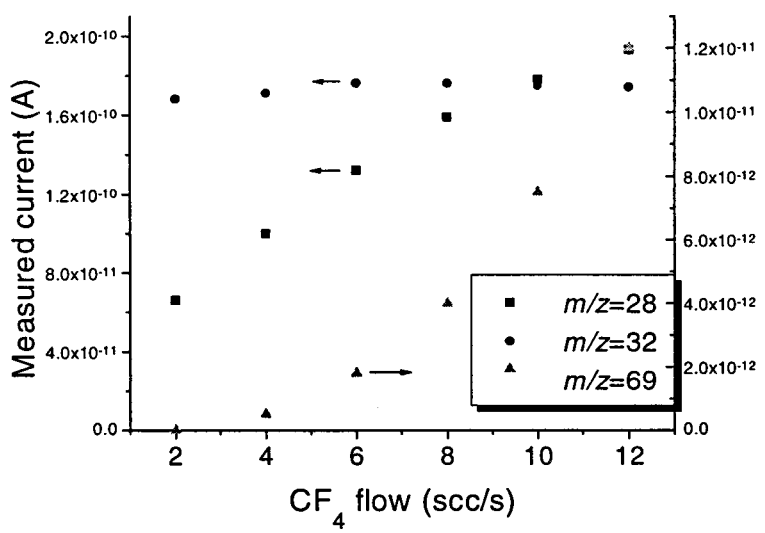

Figure 2.18: *Measurement on an $Ar/O_2/CF_4$ plasma, with variation of the CF_4 flow.*

2.8 Summary

As pointed out in section 2.5.3, it appears that SiH_2 is the main radical formed when no hydrogen is added to the arc; in this case, silane is dissociated by means of argon

ions, and increasing the arc current will lead to a higher depletion. However, when a large hydrogen flow is added, SiH_3 is the main precursor, as silane is primarily dissociated by atomic hydrogen. Disilane is also formed in the plasma, but at low concentrations, and its formation appears to be limited by the amount of silane present. Addition of deuterium instead of hydrogen gives rise to a higher depletion - however, the overall trend of the depletion versus the deuterium flow is similar to the trend with the hydrogen flow. Finally, deuterated silane is also observed, and the most likely candidate is SiH_3D.

3. Surface Reaction Probability

3.1 Introduction

This chapter describes the theory behind surface reaction probability, a method of measuring it, results under several plasma conditions, and a discussion. Chapter 3.2 begins with a description of the growth model. A method of determining the surface reaction probability experimentally, by means of deposition in a well, is illustrated in chapter 3.3. In order to gain additional understanding of the deposition profiles, a Monte Carlo simulation program was written - the basic concepts and resulting profiles of the simulations are described in chapter 3.4. Chapter 3.5 treats a method by means of which the thickness of the films deposited was measured: Electron Probe Microanalysis. The actual results, that is, surface reaction probabilities determined under a number of different plasma conditions, are listed in chapter 3.6. In chapter 3.7, finally, the obtained results are discussed, followed by a short summary in chapter 3.8.

3.2 The Growth Model and Surface Reaction Probability

Silicon atoms on the surface of a growing film have two bonds with the bulk. The other two bonds are mostly occupied by H (resulting in a hydrogen passivated surface) except for approximately one in every 10^6 - 10^8 bonds which remains free: a surface dangling bond. An SiH_3 radical can only stick to this surface, to contribute to the film growth, if it finds a dangling bond. Thus, if an SiH_3 radical were to reflect off the surface unless it happened to land on a dangling bond, its sticking probability would be of the order of 10^{-7}. However, it has been found that the probability that an SiH_3 radical sticks to the growing film is approximately 0.1. In order to find a solution for this discrepancy, Gallagher, Perrin, and Matsuda (see [ROB86], [PER89], and [MAT90]), first presented the growth model (GPM model), which describes the growth process by means of radicals which may physisorb to the surface and in this manner, due to surface mobility, have a higher probability of encountering a dangling bond.

3.2.1 The GPM Growth Model for Silane Radicals

When a particle is incident on a surface, it has three options; Figure 3.1 shows these options for an incident SiH_3 radical.

1. The particle can stick and become incorporated in the film, with probability s.
2. The particle can react with the surface to form a new volatile product (SiH_4 or Si_2H_6), with probability γ.
3. The particle can reflect off or desorb from the surface in its original form, with probability r,

The surface reaction probability β is equal to:

$$\beta = s + \gamma, \tag{3.1}$$

and the sum of all probabilities must naturally equal one:

$$s + \gamma + r = \beta + r = 1. \tag{3.2}$$

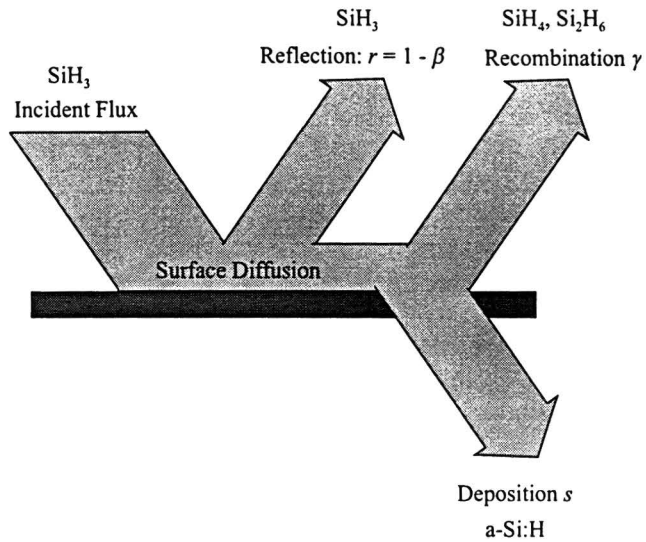

Figure 3.1: *The surface reaction probabilities.*

Under CVD-like conditions (low power and pure silane), the main radical formed is SiH_3. Doughty et. al. have found a surface reaction probability β of 0.37 ± 0.04 using slit experiments [DOU90], Gallagher has determined that $\beta \approx 0.25$ from radical diffusion and reaction equations [GAL88], and Perrin has found $\beta = 0.26 \pm 0.02$ using grid experiments [PER89]. Shaw and Tsai [SHA88] have found a surface reaction probability of 0.01 for SiH_3, but this is believed to be an erroneous result (see [DOU90] and [PER89]). All of these surface reaction probabilities pertain to a-Si:H substrates.

An SiH_3 radical has one dangling bond. When the radical collides with a hydrogen atom on the hydrogen passivated film, it will either reflect or physisorb. Once the SiH_3 radical is physisorbed to the hydrogen passivated surface, it can 'hop' from one hydrogen atom to another, until it either

- encounters a dangling bond on the surface and chemisorbs to make a strong Si-Si bond and become part of the growing film (s), or
- abstracts a hydrogen atom from the surface to form SiH_4, and returns to the gas phase (γ_a), or
- recombines with another SiH_3 radical hopping along the surface to form Si_2H_6, and returns to the gas phase (γ_r).

An additional theory is that of cross-linking, proposed by Severens et. al. [SEV95]: once the SiH_3 radical has been chemisorbed with a dangling bond, it 'wags' until one of its hydrogen atoms comes in contact with a hydrogen atom on the growing surface. These two hydrogen atoms then desorb as molecular hydrogen, and the SiH_3 radical forms a second bond with a silicon atom in the film (cross-linking).

Using laser spectroscopy techniques (LIF), Ho et. al. have found that SiH has a surface reaction probability of at least 0.94 [HO89], and the surface reaction probability of Si appears to be even closer to unity. Under PVD-like conditions, with high power and silane diluted with argon, it appears that the main radical formed is SiH_2 (silylene). Under these conditions, the surface reaction probability is approximately 0.7 ([DOU90] gives several references, based on grid experiments and photolysis). As the SiH_x ($x < 3$) radicals have two or more free bonds, they can insert themselves directly into one of the Si-H bonds on the hydrogen passivated surface: one of their free bonds accepts the surface hydrogen, thereby opening the surface Si for chemisorption with another of their free bonds (see [ZHA95] and [ZHA96]). This also means that for these radicals, the sticking probability is equal to the surface reaction probability, as they do not abstract or recombine but always stick to the surface once they have physisorbed. Thus, when these radicals are responsible for the growth of the film, there is no mechanism that selectively passivates surface dangling bonds. Another consequence is that an irregular surface, with microscopic high points and valleys, will tend to become even more irregular due to the greater probability that the radicals will strike a high point. Once these high points connect, unwanted voids, dangling bonds, and hydrogen will be incorporated in the film.

The SiH_3 radical cannot chemisorb with the surface unless it happens to collide with a dangling bond. As the density of dangling bonds is very low, physisorbed SiH_3 radicals (and possibly dangling bonds) have ample opportunity to diffuse along the surface before they meet, thereby filling in microscopic valleys and increasing the film's homogeneity (see [DOU90] for a more extensive description). For this reason, it is generally believed that deposition by means of SiH_3 radicals gives rise to higher quality films.

3.2.2 Temperature Dependence of the SiH_3 Sticking Probability

Matsuda et. al. [MAT90] have determined the surface reaction probability as well as the sticking probability of the SiH_3 radical as a function of substrate temperature by means of grid and trench experiments, cf. Figure 3.2. They have found that β is independent of temperature in the temperature range of room temperature to 480 °C - it remains constant at $\beta = 0.26 \pm 0.05$. The sticking probability is also constant, at $s = 0.09 \pm 0.02$, for lower temperatures. Above 350 °C, s starts increasing until it is equal to β around 480 °C.

The growth model explains these observations by means of hydrogen desorption. Above 350 °C, hydrogen is desorbed from the surface (two hydrogen atoms pair up to form molecular hydrogen, and leave behind two dangling bonds), thus increasing the number of dangling bonds on the surface. As the number of dangling bonds increases, a particle incident on the surface will have an increasing likelihood of encountering a dangling bond. This has two effects:

1. The probability that an incident particle reacts with the surface and sticks increases; that is, s increases.
2. The probability that an incident particle reacts with the surface to form a volatile product decreases; that is, γ decreases.

As the probability of reflection/desorption and therefore also the probability of surface reaction are not influenced by a temperature increase, and as $s + \gamma = \beta$, s will approach β as the surface temperature increases (similar to $s = \beta$ for SiH and SiH_2).

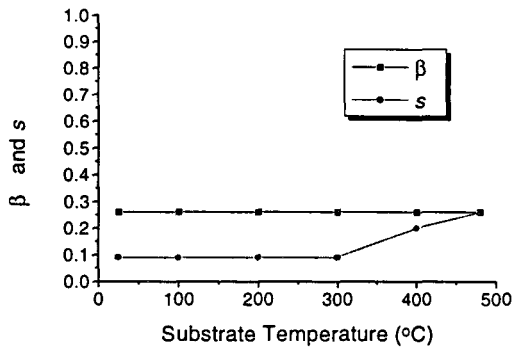

Figure 3.2: *Temperature dependence of the sticking and surface reaction probabilities ([MAT90]).*

3.3 A Method of Determining the Surface Reaction Probability

3.3.1 Introduction

Due to the possibility that a radical reflects, the 'effective' flux to a substrate is equal to $\beta\Phi$, where Φ is the flux to the substrate. If, however, the flux were to impinge on a 'black body', with zero probability of reflection, the effective flux would be equal to the actual flux, Φ. This is the basic idea behind the use of the substrate with a small slit suspended above another substrate that does *not* have a slit [DOU90]. The effective flux to the upper surface of the top sample is equal to $\beta\Phi$. Theoretically, however, the slit functions as a 'black body': the effective flux into the slit is equal to Φ. The space between these substrates is known as the well. Apart from the occasional particle that accidentally bounces back out of the well through the slit, particles entering the well are trapped; although they may reflect back and forth between the two substrates a number of times, they will eventually either react with the surface to form a gas or stick to the surface. The surface reaction probability β can then be determined by comparing the material deposited on the upper surface to the material deposited in the well.

3.3.2 The Surface Reaction Probability Deposition Setup

The surface reaction probability experiments were performed with two circular samples mounted on a special holder as shown in Figure 3.3. It consists of a base, onto which a nickel substrate is placed. This substrate forms the 'base' of the well. On top of this substrate are copper rings of various thicknesses that form the 'sides' of the well and determine its depth. The second nickel substrate (with a slit) is placed on top of these rings to form the 'cover' of the well. An aluminum ring is screwed onto the top of the stack, to keep everything in place and optimize thermal contact.

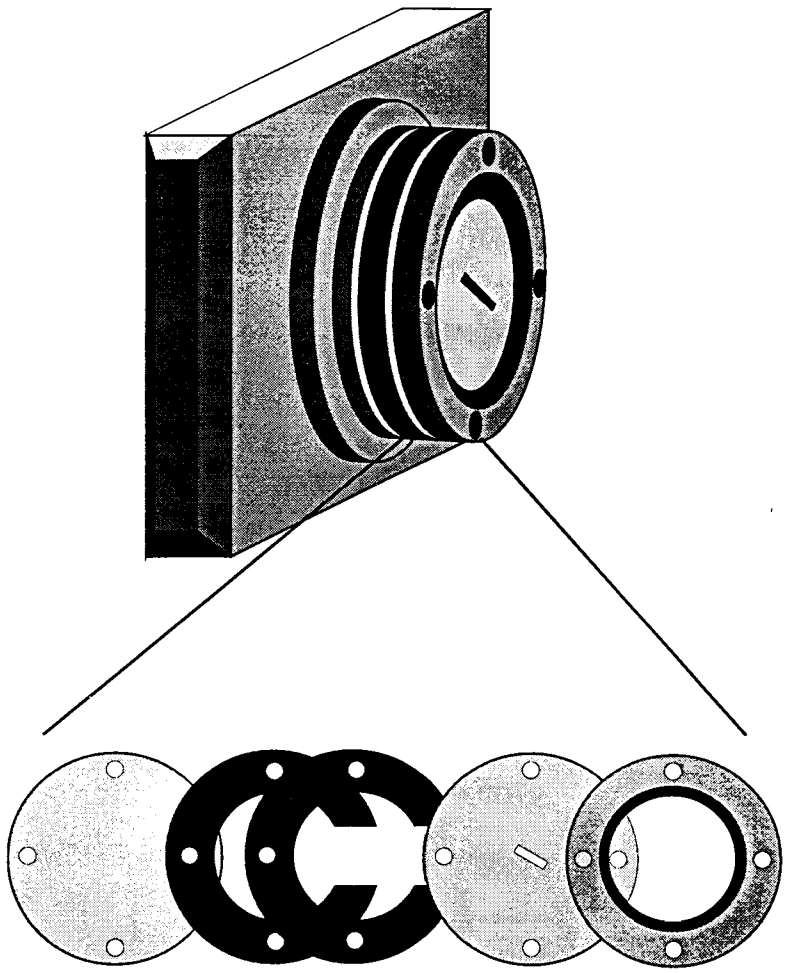

Figure 3.3: *The substrate holder for surface reaction probability experiments.*

In order for the theory described in section 3.3.1 to work, the slit must function as a 'black body'. This is the case when particles are much more likely to stick to the surface of the well than to bounce back out of the slit; in other words, when the area A_S of the slit is much smaller than the area A_W of the well, multiplied by the probability that they react with the well surface: $A_S << \beta A_W$ [DOU90].

Other size determining factors are:

1. The slit is more absorbing than the substrate, and could therefore influence the flux to the substrate right next to it. This perturbation may be neglected if the width of the slit (w) is much smaller than the mean free path for momentum transfer between radicals and silane (λ) [DOU90]. In our case, this means that w must be below 250 to 400 μm. In addition, the gas in the slit must be a Knudsen gas, see Appendix A. This means that in our case the width must be smaller than 530 μm. An additional advantage of a small slit width is that it reduces the bounce-out from the well.
2. In order to avoid deposition on the sides of the slit, the upper substrate must be very thin, at most approximately 1/4 of the slit width. That means that it may be between 50 and 100 μm thick.

3. Deposition on substrates with a large diameter will give rise to a better homogeneity, as the substrates are clamped farther from the slit. Also, deposition on the sides of the well will be less likely with a larger well diameter, and a larger well will increase the effectiveness as a 'black body' (see section 3.3.1). However, the diameter is limited by mechanical strength - if the substrates become too large, the upper substrate may sag or even rip when exposed to the plasma beam.

A slit width of 250 μm was decided upon, automatically limiting the thickness of the upper substrate to 50 μm. The length of the slit is irrelevant, and was chosen to be 7.5 mm. Similarly, the thickness of the lower substrate is also unimportant; these were made 100 μm thick, for strength and ease of handling. The effective diameter (that is, the diameter of the well), was chosen to be 3 cm.

Concerning the sides of the well:

- It is inevitable that the upper substrate will have a higher temperature than the lower, as it is directly exposed to the plasma beam and isolated from the lower substrate by the sides of the well. However, to minimize this problem, the rings that make up the sides of the well are wide and made of copper to ensure maximal thermal conduction. Results of temperature measurements are listed in Appendix B.
- The depth of the well is determined by the number of and thickness of the copper rings. These vary in thickness from 0.1 mm. to 2 mm. The depth of the well must be large enough to minimize "bounce-out", but small enough to avoid deposition on the sides of the well. In addition, the gas in the well must be a Knudsen gas, so that particles do not interact. In order to comply to this (see Appendix A), the height of the well must also be less than 500 μm*.
- The copper rings do not form complete circles but have a gap. In this way, there is an open connection between the well and the outside, in the vacuum chamber. This is to avoid a large pressure difference between the inside and the outside of the well, when the plasma beam is directed at the top of the well.

The dimensions of the substrates are shown in Figure 3.4. The copper rings have an outer diameter of 5 cm. and an inner diameter of 3 cm., thereby creating a well with a diameter of 3 cm.

* This was only realised after some time, when a number of experiments had already been performed with larger well depths.

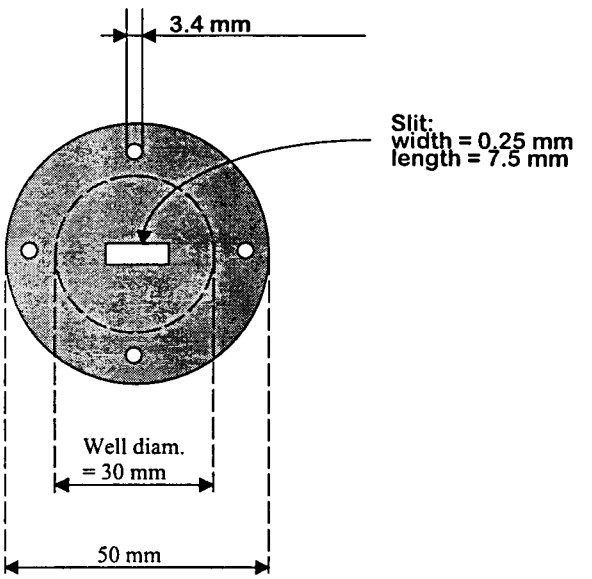

Figure 3.4: *The surface reaction probability substrate dimensions.*

T_{wb} and T_{wt} are defined to be the volumes of material deposited on the base and the top of the well, respectively, as shown in Figure 3.5. This means that the total volume of material deposited in the well is equal to $T_w = T_{wb} + T_{wt}$. The quantity t_s is defined to be the thickness of the film deposited on top of the upper sample (directly exposed to the plasma beam).

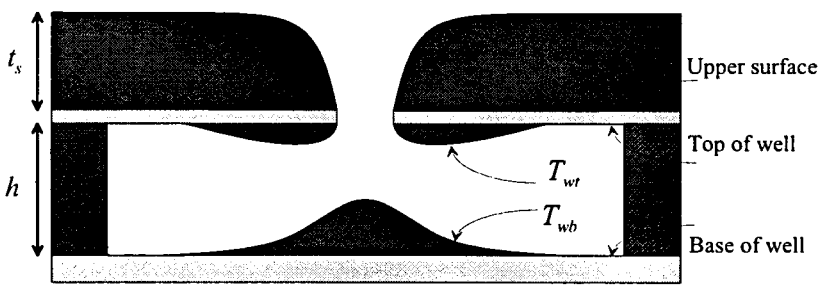

Figure 3.5: *Deposition in the well (not to scale).*

During temperature measurements, a thermocouple was inserted into the aluminum sample holder just below the lower nickel substrate, and another thermocouple was glued to the underside of the upper nickel substrate. In this way, the temperature of both substrates when exposed to various types of plasmas could be monitored and compared to the yoke temperature. The results of these measurements are given in Appendix C. These experiments showed that the temperature of the samples increases less due to exposure to a plasma if their initial temperature is higher, and that the type of plasma is an important factor in the heating of the samples - a plasma with silane results in a lower temperature than a plasma without silane, as the sample can lose more heat through radiation because of the roughness and dark color of the silicon deposition.

3.3.3 Determination of Fractional Distribution of Deposition

From comparison of the amount of material deposited at the base of the well to that deposited at the top of the well, and comparison of what is deposited in the well to what is deposited on the upper surface, two simple equations can be deduced. First of all, let us assume that the two surfaces (the base and the top of the well) do not necessarily have the same coefficients: the base of the well has coefficients s, γ, and r with subscript 'b', whereas the top of the well has coefficients with subscript 't'.

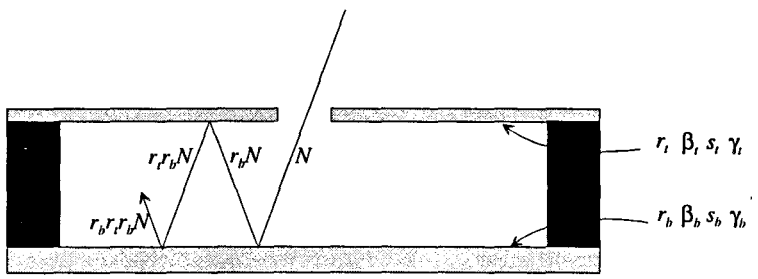

Figure 3.6: *Reflection in the well.*

Now, let N particles enter the well through the slit. Upon first impact with the base of the well,
s_bN particles will stick,
γ_bN particles will react to form a volatile product and dissapear from the system,
r_bN particles will reflect/desorb from the surface and go on to the top of the well.

When these r_bN particles reach the top of the well, as shown in Figure 3.6, they react and
s_tr_bN particles will stick,
γ_tr_bN particles will disappear from the system,
r_tr_bN particles will reflect and return to the base of the well,
and so forth.

The number of particles that sticks to the base of the well is then equal to:

$$s_bN + s_br_tr_bN + s_br_tr_br_tr_bN + \cdots = s_bN\sum_{n=0}^{\infty}(r_tr_b)^n = \frac{s_bN}{1-r_br_t}. \tag{3.3}$$

This means that a fraction $s_b/(1- r_tr_b)$ of all particles that enters the well sticks to the base of the well to form a film. Similarly, the fraction of particles that sticks to the top of the well is $s_tr_b/(1- r_tr_b)$.

Of all the particles that enter the well, the fraction that sticks *somewhere* (either to the top or to the base) in the well is equal to:

$$\frac{s_b}{1-r_br_t} + \frac{s_tr_b}{1-r_br_t} = \frac{s_b+s_tr_b}{1-r_br_t}. \tag{3.4}$$

On the other hand, the ratio of particles sticking to the base of the well to particles sticking to the top of the well is equal to:

$$\frac{\text{Particles sticking to bottom}}{\text{Particles sticking to top}} = \frac{\frac{s_b}{1-r_b r_t}}{\frac{s_t r_b}{1-r_b r_t}} = \frac{s_b}{s_t r_b}. \tag{3.5}$$

3.3.4 The Flux Entering the Well

In order to be able to compare the deposition in the well to the deposition on top of the upper substrate, the flux entering the well must be calculated (see [DOU90]). If the flux of particles incident on the top of the upper substrate per unit area is equal to F (particles/m^{2}s) then the number of particles that *sticks* to this surface is equal to $g_s = s_t F$ (particles/m^{2}s), as the fraction of particles that sticks to the upper surface is simply s_t. After τ seconds of deposition, the film thickness on top of the upper surface is equal to:

$$t_s = g_s \tau = s_t F \tau . \tag{3.6}$$

The slit was designed such that it has no influence on the flux to the upper surface near the slit. Then the flux of particles entering the well through the slit is equal to FA_S. Using the fraction of particles that sticks in the well derived in equation (3.4), this means that the total film growth rate in the well is equal to:

$$G_w = FA_S \cdot \frac{s_b + s_t r_b}{1 - r_b r_t}, \tag{3.7}$$

in (particles/s). Then, the deposition in the well totals:

$$T_w = G_w \tau = FA_S \cdot \frac{s_b + s_t r_b}{1 - r_b r_t} \cdot \tau, \tag{3.8}$$

after τ seconds of deposition. Combining with equation (3.6) leads to:

$$\frac{T_w}{t_s A_S} = \frac{s_b + s_t r_b}{1 - r_b r_t} \cdot \frac{1}{s_t}. \tag{3.9}$$

As the ratio of particles sticking to the base of the well to particles sticking to the top of the well is equal to T_{wb}/T_{wt}, equation (3.5) can be rewritten as:

$$\frac{T_{wb}}{T_{wt}} = \frac{s_b}{s_t r_b}, \tag{3.10}$$

or

$$s_b = \frac{T_{wb}}{T_{wt}} \cdot s_t r_b . \tag{3.11}$$

This can be used to simplify equation (3.9), by eliminating s_b:

$$\frac{T_w}{t_s A_S} = \frac{\frac{T_{wb}}{T_{wt}} s_t r_b + s_t r_b}{1 - r_b r_t} \cdot \frac{1}{s_t} = r_b \frac{\frac{T_{wb}}{T_{wt}} + 1}{1 - r_b r_t}, \tag{3.12}$$

$$\frac{T_{wb} + T_{wt}}{t_s A_S} = \frac{r_b}{T_{wt}} \frac{T_{wb} + T_{wt}}{1 - r_b r_t}, \tag{3.13}$$

which finally simplifies to:

$$\frac{T_{wt}}{t_s A_S} = \frac{r_b}{1 - r_b r_t} . \tag{3.14}$$

After deposition of a film, the film thickness on top of the upper surface (t_s) and the deposition in the well (T_{wb}, T_{wt}, and $T_w = T_{wb} + T_{wt}$) can be determined. The area of the slit is always the same and therefore also known. Thus, the two equations (3.11) and (3.14) describe the relationship between four unknowns (s_b, s_t, r_b, r_t): two additional equations will have to be found. In the next two sections, two possibilities of solving this problem will be treated.

3.3.5 Equal Sticking Probabilities at the Top and Base of the Well

As discussed in section 3.2.2, the sticking probability does not depend on the temperature as long as the surface temperature remains below 350 °C (according to Matsuda's growth model). Therefore, the sticking probability for the top and the base of the well are equal, as long as both remain below this critical temperature. This is the method utilized by Doughty [DOU90]. This gives rise to two additional equations:

$$\left.\begin{aligned} s_b &= s_t = s \\ r_b &= r_t = r \end{aligned}\right\} . \tag{3.15}$$

This automatically implies that $\beta_b = \beta_t = \beta$, and $\gamma_b = \gamma_t = \gamma$. Equation (3.11) can then be simplified to:

$$s = \frac{T_{wb}}{T_{wt}} \cdot s r \quad \rightarrow \quad r = \frac{T_{wt}}{T_{wb}} . \tag{3.16}$$

Equation (3.9) then reduces to:

$$\frac{T_w}{t_s A_s} = \frac{1 + r}{1 - r^2} = \frac{1}{1 - r} = \frac{1}{\beta} . \tag{3.17}$$

Thus, once the film thickness on top of the upper substrate is known, as well as the total volume of deposition in the well, β can be calculated, and r can then be found using $r = 1-\beta$. The quantities s and γ, however, cannot be determined. Note that the requirement that $\beta \leq 1$ automatically leads to $t_s A_s \leq T_w$.

3.3.6 Top Substrate Temperature Exceeds Critical Temperature

If the substrates do not have the same temperature, and if the temperature of the upper substrate exceeds the critical temperature where s is no longer a constant (unless the initial temperature of the substrates is extremely high, the upper substrate will always have a higher temperature as it is directly exposed to the plasma beam - see Appendix C), a different assumption can be made, namely that on the upper substrate (the top of the well) $s_t \approx \beta_t$, and $\gamma_t \approx 0$. As the probabilities of reflection/desorption r and of surface reaction β are temperature independent and therefore the same for both substrates, the two additional equations are:

$$\left.\begin{aligned} r_b &= r_t = r \\ s_t &= \beta_t = 1-r \end{aligned}\right\}. \tag{3.18}$$

Equation (3.14) then becomes:

$$\frac{T_{wt}}{t_s A_S} = \frac{r}{1-r^2}, \tag{3.19}$$

which can be solved for r:

$$r = \frac{-1+\sqrt{1+4Q^2}}{2Q}, (0 \leq r \leq 1), \tag{3.20}$$

where Q is defined as $Q = T_{wt}/t_s A_s$. The second solution of the quadratic equation is not relevant, as it would lead to a negative r, and r must lie between zero and one. A plot of r versus Q is shown in Figure 3.7. The quantity s_t can then be calculated from equation (3.18), and s_b can be found from (see equation (3.11)):

$$s_b = \frac{T_{wb}}{T_{wt}} \cdot s_t r. \tag{3.21}$$

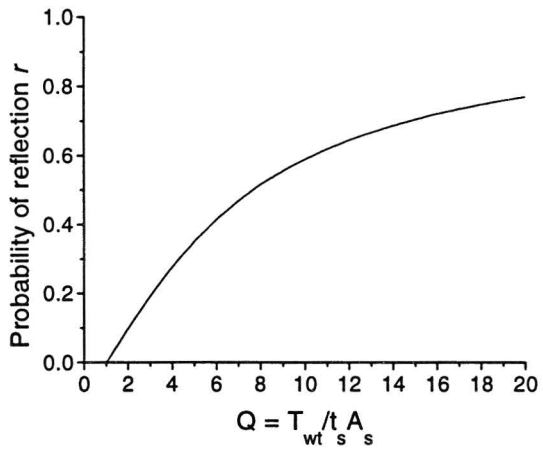

Figure 3.7: *r versus Q.*

3.4 Monte Carlo Simulation Program of the Slit Experiment

3.4.1 Basic Concepts of the Simulation

The equations in sections 3.3.3 through 3.3.6 describe the amount of material that will stick in the well compared to that which will stick to the upper surface, and they describe the fractional distribution of material between the base and the top of the well. Nothing is known on the thickness profiles, however. To analyse the profile shapes and the influence of sticking probabilities and angular distributions on these shapes, a Monte Carlo simulation program was developed. The simulation program, written in Turbo Pascal, generates a particle somewhere in the slit in the upper sample, in the experiment described in section 3.3.1. This particle has a random position (a pair of x,y coordinates) within the area of the slit, as well as a random incoming angle (an angle φ corresponding to the x-direction and an angle θ corresponding to the y-direction). This setup is shown in Figure 3.8.

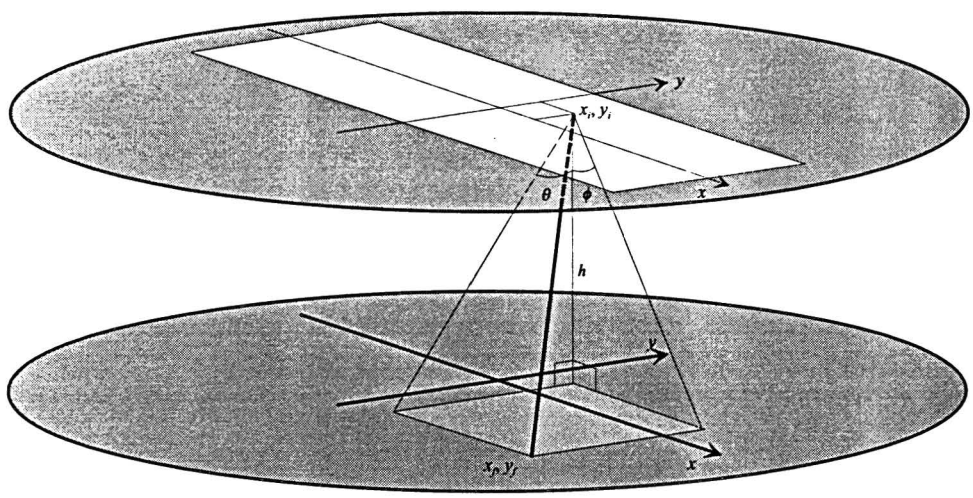

Figure 3.8:*Generation of particles in the slit.*

From there, knowing the height of the well, the position at which the particle will land on the base of the well is calculated, using

$$x_f = x_i + h\tan\varphi$$
$$y_f = y_i + h\tan\theta. \qquad (3.22)$$

Next, another random generator is used to determine whether the particle sticks - the sticking probabilities for the top and the base of the well are considered 'known'. The γ option (abstraction or recombination) is not included in the program. Also, it is assumed that particles cannot interact, that is, that the mean free path of particles in the well is larger than the well height. If the particle does not stick, it 'reflects' off the base of the well from position (x_f, y_f) with another pair of newly generated angles of departure. The position at which it will 'land' at the top of the well is then calculated, and once again it is determined whether the particle sticks. This procedure is repeated until the particle sticks upon landing on either the base or the top of the well, after which the position of the particle is stored, resulting in a film thickness profile, with thicknesses in atoms/cm^2.

In order to be able to compare simulation results to measured results, the program determines the number of particles that must enter the well from the requested thickness (the value of t_s of a measurement) on top of the upper surface and the sticking probability of the top of the well.

3.4.2 The Angles of Incidence and Reflection

It is assumed that the angles at which the particles enter the well are distributed according to the cosine law (the slit is assumed to be a line, and the particles approach it with an isotropic distribution), although this can also be varied in the program. However, the distribution of angles at which particles come off the surface of the well is not known, and depends on whether the particle forms a temporary bond with the surface atoms (see [YUN95]).

- Cosine re-emission: the incoming particle has strong interaction with the surface so that all information on its incoming angle is lost. The probability of a certain re-emission angle ϕ is proportional to $\cos(\phi)$, where ϕ is the angle relative to the surface normal. The result is that angles close to 0° are most likely to occur.
- Specular reflection: the angle of reflection is equal to the incident angle. This implies simple elastic collision of the incoming particle with a perfectly reflecting surface.
- Diffuse re-emission: the probability that a particle reacts is the same in all directions, independent of the angle of reflection as well as the incident angle.

Most researchers and Monte Carlo programmers assume that the re-emission angles are distributed according to the cosine law, or have found that this best fits their results; see [MAT90], [HO89], and [ZHA95], for example. As the re-emission mechanism in our case is not known, several different angular distributions were tried out.

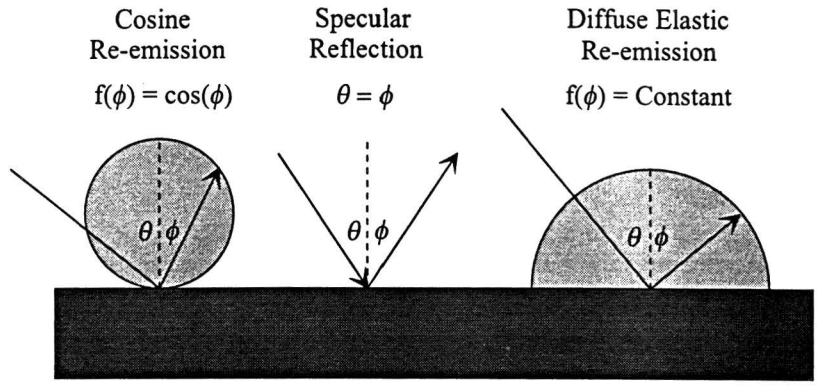

Figure 3.9: *Re-emission mechanisms of radicals reflecting off the growing film.*

3.4.3 Operation of the Monte Carlo Program

The Monte Carlo program's main outline is given in the flowchart in Appendix G. Whether a particle has stuck to the top or the base of the well is determined by keeping track of the number of times that it *did not* stick, i.e., the number of times it reflected.

The program requires the following input:

- Height of the well,
- Sticking probability for the top and the base of the well, in percentages,
- Film thickness on top of the upper substrate,
- Angular distribution upon reflection and for incoming particles,
- Number of particles in a cluster

The output to the screen is:

- The number of particles that stuck to either the top or the base of the well, but outside of the grid, and was not counted,
- The number of particles that left the well through the slit (bounce-out), and was not counted,
- The number of particles that was counted.

3.4.4 Typical Monte Carlo Profiles

The thickness profiles for clusters of radicals entering the well through the slit were calculated for a large variety of different sticking probabilities and angular distributions. A typical result is shown in Figure 3.10. The values of the parameters put into this simulation are summarized in Table 3.1. Figure 3.10 (a) and (b) show the 3-dimensional profile for the base and top of the well, respectively, whereas Figure 3.10 (c) and (d) show a contour plot of these same profiles.

Table 3.1: *Values of parameters used in the Monte Carlo simulation in section 3.4.4.*

Description	Symbol	Value
Sticking probability top of well	s_t	0.6
Sticking probability base of well	s_b	0.6
Distribution incoming angles		cosϕ
Distribution re-emission angles		cosϕ
Thickness on upper surface	t_s	700 nm
Height of well	h	0.5 mm

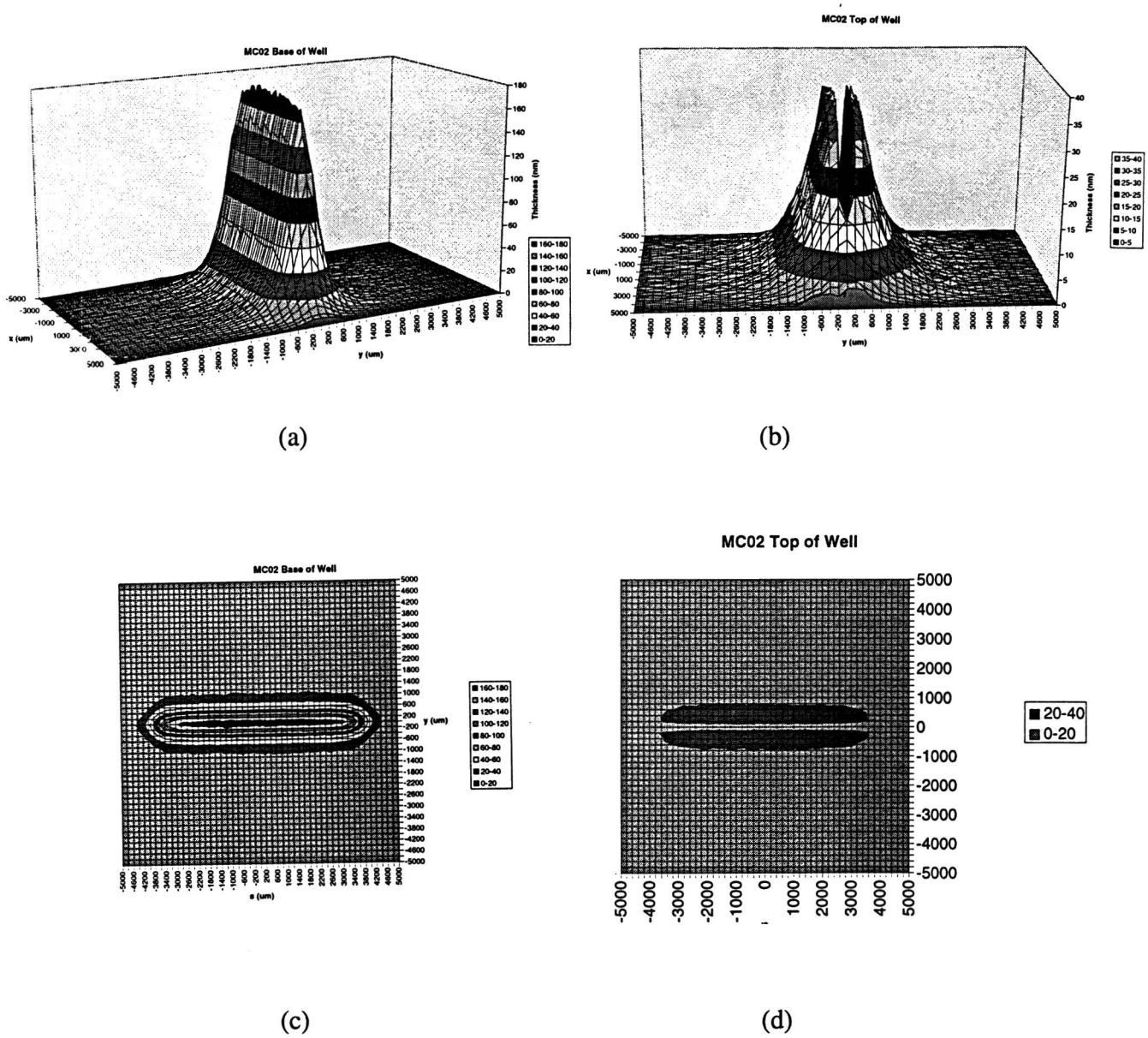

(a) (b)

(c) (d)

Figure 3.10: *Profiles obtained from Monte Carlo simulation using the parameters in Table 3.1.*

The transverse cross-section of these profiles can be closely approximated with a Lorentz curve, as is shown in Figure 3.11, for the base and the top of the well.

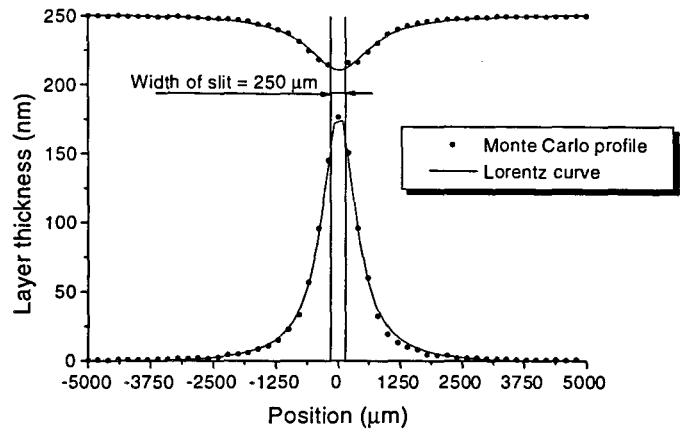

Figure 3.11: *Lorentz curve of the profiles obtained from Monte Carlo simulations.*

In the profile of the top of the well in Figure 3.11 the point exactly in the middle, which lies in the slit (and where the thickness is, naturally, zero) has been removed prior to making the Lorentz fit. As the volume that is then added to the total represents the volume that bounced out of the well, a correction for the bounce-out (intrapolation) is automatically made in this manner.

The width of the slit (roughly) has been added to the figure, for comparison. Figure 3.12 shows the longitudinal cross-section of the same Monte Carlo profile.

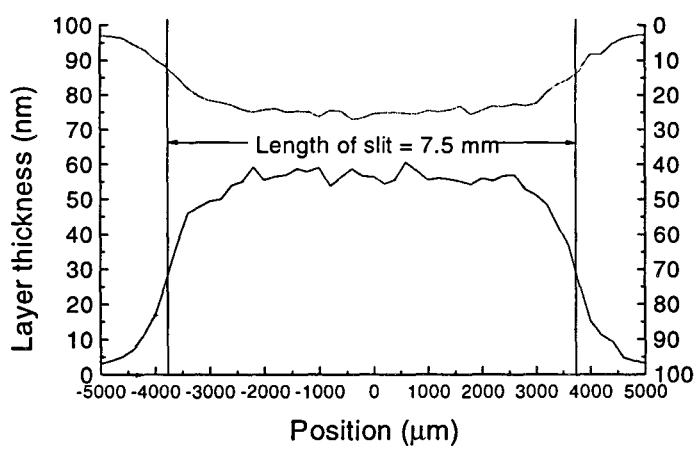

Figure 3.12: *Longitudinal cross-section of the Monte Carlo profiles, as compared to the length of the slit.*

3.4.5 The Effect of Sticking Probability on the Profile

The effect of the sticking probability on the profiles in the well was determined for two different cases: equal sticking probabilities for the top and the base, and a higher sticking probability for the top of the well. The effect of a varying overall sticking probability is shown in Figure 3.13, for the case where the sticking probability at the top of the well is the same as that at the base: $s_t = s_b = s$. Both the incoming angles and the angles of reflection were distributed according to the cosine law.

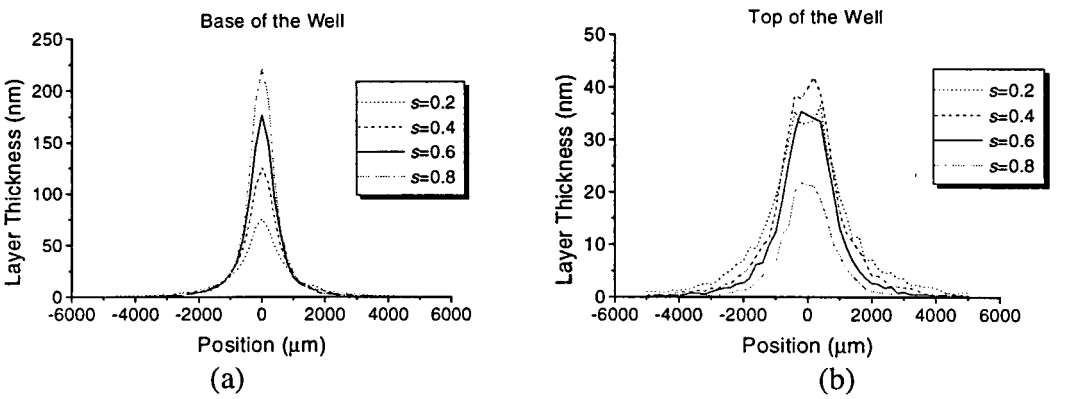

Figure 3.13: *Effect of the sticking probability on the profiles in the well; equal s (s = 0.2, 0.4, 0.6, 0.8) for the top and base.*

To demonstrate the effect of a higher sticking probability at the top of the well, s_t was varied while s_b was kept constant. The incoming and re-emission angles were once again distributed according to the cosine law. The results are shown in Figure 3.14.

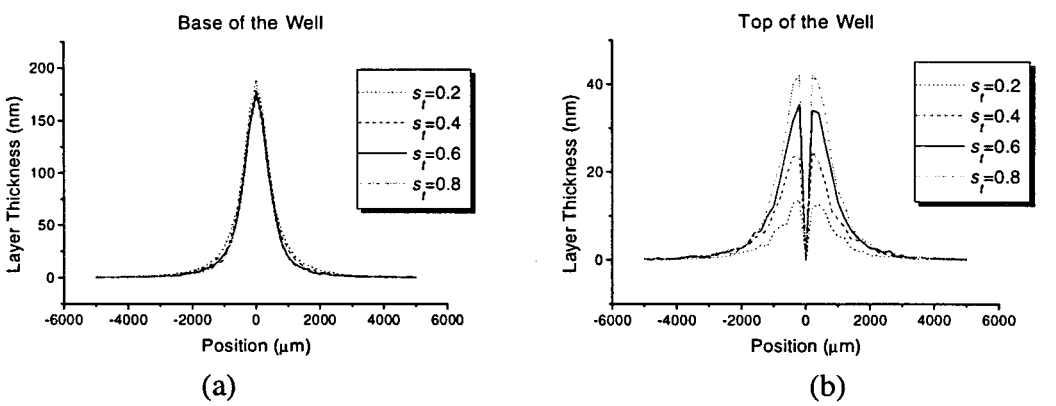

Figure 3.14: *Effect of s_t (s_t = 0.2, 0.4, 0.6, 0.8) on the profiles in the well; s_b is kept constant at 0.6.*

These results indicate the following: if both substrates have equal sticking probabilities, a high s will result in most particles sticking to the base of the well at first impact - the thickness at the base of the well will be very high compared to that at the top of the well. In the limit of the sticking probability going to one, all deposition will be at the base. On the other hand, in the limit of s going to zero, the differences in

the profiles between the top and the base of the well will disappear. There can, however, *never* be more deposition at the top than at the base of the well, as particles that reach the top of the well have already been through one reflection.

If the sticking probability at the upper substrate is high compared to that of the lower, then the deposition at the top of the well will increase, compared to that at the base of the well, as s_t becomes larger. In this case, the total deposition at the top *can* exceed that at the base.

3.4.6 The Effect of the Incoming/Re-emission Angular Distributions on the Profile

Although it is expected that particles enter the slit with a cosine angular distribution, the profile with a random distribution of the incoming angle was also calculated, for completeness. In Figure 3.15, the effect of the incoming and the re-emission angular distribution is shown. The angular distributions corresponding to the four simulations are summarized in Table 3.2. The other parameters were defined as in Table 3.1: the sticking probabilities at the top and bottom of the well were both 0.6.

Table 3.2: Angular distributions corresponding to the Monte Carlo simulations in Figure 3.15.

Simulation	Incoming	Re-emission
MC01	cosϕ	random
MC02	cosϕ	cosϕ
MC03	random	random
MC04	random	cosϕ

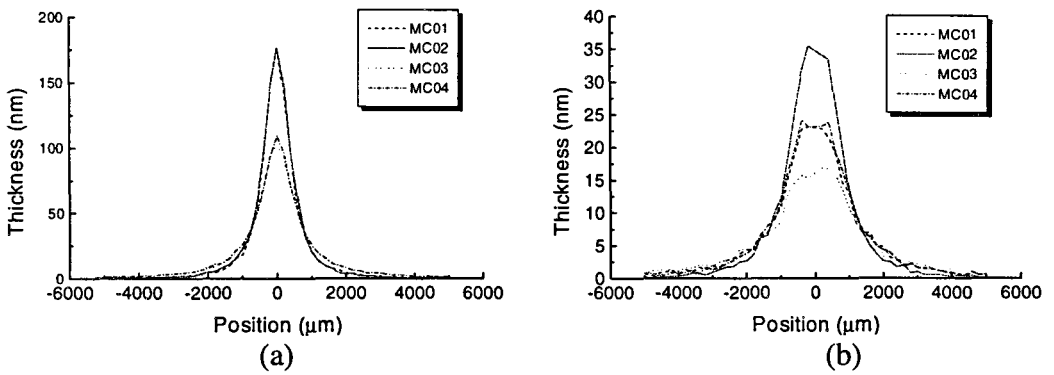

Figure 3.15: *Effect of incoming and re-emission angular distributions on the profiles in the well.* $s_t = s_b = 0.6$.

Apparently, the profile at the base of the well is determined mainly by the distribution of the incoming angle. This is due to the fact that the sticking probability is high (s = 0.6) on both substrates, so that few particles will stick to the base after having

reflected, as this means that they would have had to 'survive' two reflections. The profile for random angles of incidence is wider than for a cosine distribution, which is perfectly understandable as the cosine law favors small angles. Note that the integrated volumes are all equal.

The profile at the top of the well is more complicated, as particles have always had at least one reflection to get there. However it is obvious that the profile for particles that have entered the well with a cosine distribution and that reflect with a cosine distribution is the most narrow, whereas the profile with two random distributions is the widest. The other two profiles are nearly identical, which means that whether the particles enter with one angular distribution and reflect with the other, or vice versa, does not make any difference. Here, once again, the fact that the majority of the particles does not reflect more than twice is essential. If the particles would have a lower sticking probability, the number of reflections would become much larger and there would be a difference between MC01 and MC04. The reason that the profiles at the top of the well look much 'rougher' than those at the base of the well is that the number of particles that sticks here is much smaller, thereby reducing the resolution.

The angular distribution is not relevant for determination of the surface reaction probability, as only deposition volumes and not the profiles are used in the calculation of β. In general, the shape of the profiles generated by means of the Monte Carlo simulation is similar to the profile shape of the actual depositions, as will be seen in chapter 3.6 - both appear to be Lorentz curves. Note that neglecting γ gives rise to an error in the relative profiles at the top and base of the well: if γ is included, $r = 1 - s - \gamma$. If it is neglected, such as is the case in the results presented in this chapter, $r = 1 - s$, so that the deposition at the top of the well is overestimated.

3.5 Determination of Film Thickness by means of EPMA

3.5.1 Introduction

Determination of the film thickness of silicon on nickel substrates was performed by means of X-ray microanalysis in an electron probe microanalyzer (EPMA). An EPMA is a machine similar to a scanning electron microscope (SEM) in that they are both based on directing an electron beam at a sample and observing the effects. However, whereas the SEM is designed to produce images of a sample by looking at secondary and backscattered electrons (micro*scope*), the EPMA is optimized for analyzing the resulting radiation (micro*analyzer*). The EPMA is also capable of producing images, but these are of lesser quality. In our case, the EPMA was used to analyze the thickness of the silicon film on top of the nickel substrate. The basic principle consists of detecting the characteristic silicon and nickel X-rays that are produced when a sample is bombarded with high energy electrons, by means of wavelength dispersive spectroscopy (WDS). The raw results were transformed into silicon film thicknesses with the Thin Film Analysis (TFA) program.

3.5.2 X-ray Production

When an electron collides with an atom in the material, it can release an electron from one of the atom's shells. An electron from a higher shell then deexcites to fill in the

space, and in the process a specific X-ray is emitted [FRI]. This X-ray is named in such a way that the capital letter refers to the shell the electron drops down to, and the Greek letter refers to the shell this electron came from. If, for example, a K-shell electron is repelled from the atom and it is replaced by an L-shell electron, then Kα X-radiation is emitted. If, on the other hand, the repelled electron is replaced by an M-shell electron, then Kβ-radiation is emitted. Every element gives a *characteristic* spectrum of X-rays, from which it can be identified.

The very light (low atomic number) elements only have K lines as they have no L-shell. In fact, hydrogen and helium cannot be detected at all, as there is no second shell from which electrons can deexcite to replace the ejected electron.

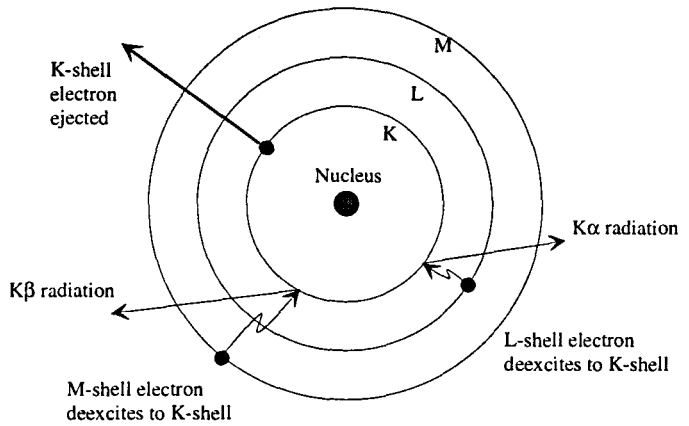

Figure 3.16: *X-ray production using the Bohr model of the atom.*

3.5.3 X-ray Detection by means of WDS

Not only is the X-ray's energy element- and transition-specific, its wavelength is also. Therefore, X-rays can be detected with two different kinds of detectors (spectrometers):
EDS = Energy Dispersive Spectroscopy, and
WDS = Wavelength Dispersive Spectroscopy.

The Jeol EPMA used is equipped with both types of spectrometers. WDS will be described briefly as this is the technique we used; the reader is referred to [FRI] and [GRI93] for a description of EDS and further details on WDS. In WDS, X-rays entering the spectrometer pass through an analyzing crystal before reaching the detector. This crystal diffracts the X-rays according to Bragg's law:

$$n\lambda = 2d\sin\theta. \tag{3.23}$$

Therefore, the detector can be placed at such an angle to the crystal that it will only detect X-rays of a certain specific wavelength. Once the elements in the sample are known, and the precise location of their main peak (usually the Kα) is located, the detector can be set to measuring X-rays with this wavelength only. The EPMA has 5 detectors; if, such as in our case, only two elements are being measured (Si and Ni),

one of the detectors is programmed to measure at the wavelength of silicon's Kα-line, and another to measure at the wavelength of nickel's Kα-line. The other detectors then remain inactive.

3.5.4 Determination of Film Thickness

The basic concept of quantitative electron probe microanalysis, developed by Castaing, is comparison of the generated X-ray intensity from a certain element in an unknown to the X-ray intensity of that same element generated in a standard containing a known amount of the element. When making use of this technique, the system must first be calibrated and the standard intensity must be determined. First, the 'standard' sample (in our case, pure silicon or pure nickel) is placed in the EPMA. After the exact wavelength of the peak to be measured has been found, and the background has been subtracted, the 'standard' peak intensity is determined by counting the number of counts during a certain time interval. This calibration is done for all (or, in our case, both) elements.

After calibration, the 'unknown' sample is placed in the EPMA. The electron beam is focused at a spot on the sample, and X-rays will escape from the silicon film and the nickel bulk underneath. The two spectrometers directed at the sample, one set to measure silicon's Kα-line and the other nickel's Kα-line, then measure the intensity of the incoming X-rays. The background is subtracted once again. If the silicon intensity is divided by that of the standard, measured under the same angle and with the same electron energy, the result is the so-called silicon k-ratio:

$$k_{Si} = \frac{I_{\text{unknown}}}{I_{\text{standard}}}. \tag{3.24}$$

The same is done for nickel. Thus, a pair of k-ratios is determined at a certain position (at the spot of the electron beam). By moving the sample, these k-ratios can be determined for a large number of positions on the sample; the result is a list of sample-positions, with a pair of k-ratios at each position.

Ideally, the silicon k-ratio would be equal to the elemental concentration (in wt%) of silicon in the unknown (and similarly for nickel). However, a number of corrections must be made, for:

- The atomic number - differences in the electron scattering and penetration for the sample and the standard,
- The absorption - difference in the absorption of the X-rays as they pass through the standard or sample to the detector, after generation,
- The secondary X-ray production (fluorescence factor) - those X-rays that were not generated by the electron beam but by other X-rays previously released from the atoms.

These corrections (according to the PROZA method) are performed in the software program Thin Film Analysis (TFA). See [BAS93] for a description of the method according to which this is done. The result is a mass thickness of silicon (in kg/m^2).

In this manner, if a scan is made perpendicularly to the long side of the slit, the mass thickness profile of the silicon film on top of the nickel bulk can be determined. From

this, the silicon film thickness can be calculated by dividing by the density of crystalline silicon. The silicon film thickness versus the silicon k-ratio is shown in Figure 3.17: (a) shows the dependency for low k-ratios whereas (b) shows the dependency for high k-ratios.

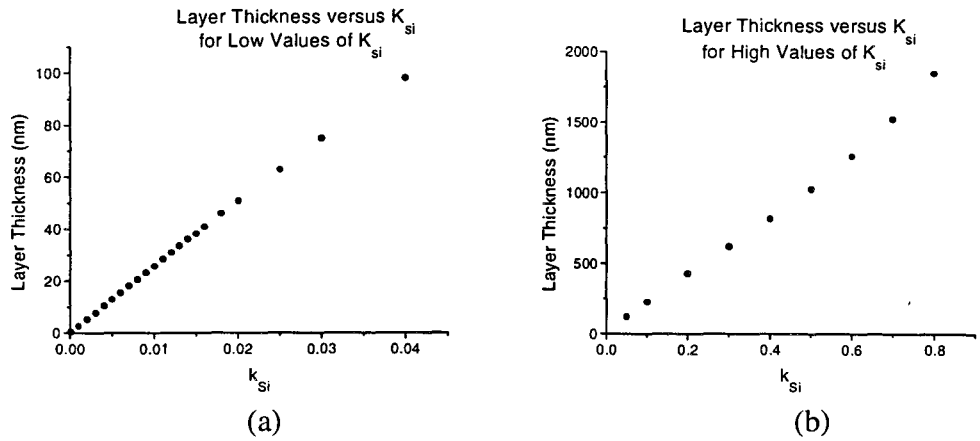

Figure 3.17: *Silicon film thickness as a function of the silicon k-ratio, for low and for high k-ratios.*

3.5.5 Effects of a Distorted Sample

When a scan is made of the sample, the sample is made to move along a path perpendicular to the slit. If the sample is not flat but distorted, assuming a linear variation in z will result in the detector being out of focus for part of the linescan, see Figure 3.18. This results in an error in the measured signal - in fact, it means that if the signal appears to be irregular, the only points that are completely trustworthy are the beginning and endpoints of the linescan, as the detectors were focused at these points.

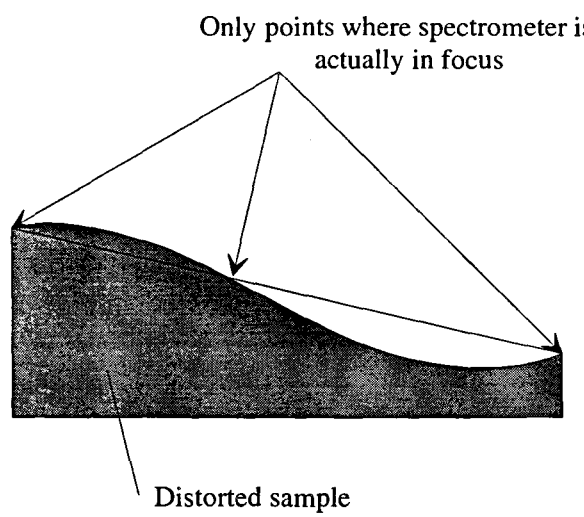

Figure 3.18: *Error due to bad focus in a distorted sample.*

The second source of error also lies in the fact that the sample may be distorted; this time, however, the problem lies in the absorption of X-rays as they leave the sample. As shown in Figure 3.19, one detector (the one set to measure X-rays from silicon, for instance) is on one side of the sample, whereas the other detector is diametrically opposed. Then, if the sample is tilted, X-rays headed toward one detector will face a longer path inside the sample than X-rays headed toward the other detector; the result is that one detector receives a signal of smaller intensity, due to greater absorption in the film. In Figure 3.19, X-rays heading for the silicon detector will be absorbed more than X-rays heading for the nickel detector. Consequently, the silicon intensity measured is too low, resulting in a measured silicon film thickness that is too low. This effect is only seen when the distortion is significant.

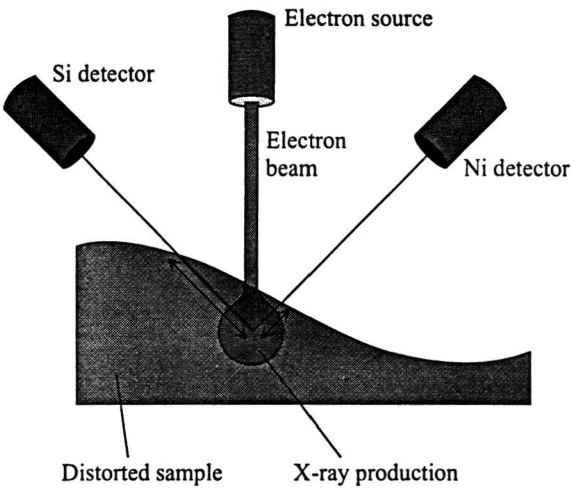

Figure 3.19: *Error due to differences in path lengths out of the sample, in a distorted sample.*

3.5.6 Types of Samples Suitable for EPMA

Film analysis as described above is not possible for all types of films and substrates. If analysis is done on silicon films, the substrate may **not** be (crystalline) silicon, as no distinction can then be made between X-rays coming from the substrate and those coming from the film. As the Expanding Thermal Plasma Deposition setup is also used for the deposition of carbon, it may at some time in the future also be interesting to analyze the thickness profile of carbon films deposited through a slit. However, EPMA analysis of carbon films is far more difficult than analysis of silicon films, for two reasons. First, detection of X-rays from lighter materials is more difficult than from heavier materials, and carbon's atomic number is only 12. Secondly, residual hydrocarbons in the EPMA vacuum chamber are broken down by the electron beam so that carbon is actually deposited on any sample that is being observed. This is no problem if the detectors are set to measuring silicon X-rays, but if the signal of carbon is being measured, then the signal will slowly rise during measurement, and special precautions have to be taken. Finally, the substrate must be a conductor: if not, the electron beam will give rise to a build up of electrons in the substrate. This negative charge will then influence the penetration depth of the electron beam.

3.6 Slit Experiment Results

3.6.1 Slit Experiment Depositions

Depositions on the substrate setup as described in section 3.3.2 were performed under a number of different conditions, summarized in Table 3.3.

Table 3.3: *Deposition conditions of the surface reaction probability experiments.*

Samples	Height of Well (mm)	H_2-flow (scc/s)	SiH_4-flow (scc/s)	Yoke-temp. (°C)	Depo-time (min.)	Depletion (%)
SP001	3.3	10	20‡	150	1	
SP002*	3.3	10	20	320	3	
SP003*	1	10	20	310	2	
SP005	0.5	10	20	30	3	
SP009	1	10	20	100	3	
SP010	1	0	20	130	0.5	
SP011†	1	10	10	200	2	
SP012†	1	10	10	200	2	
SP013	1	10	10	200	3	22.6
SP014†	0.5	10	10	200	3	22.7
SP015	0.5	0	2	100	1.5	98.7
SP016	0.5	5	2	100	2	45.2
SP017	0.5	1	2	100	4	94.7

Measurement SP004 was on a regular wafer, samples SP006 and SP007 were used for carbon deposition, and sample SP008 was used for the temperature measurements described in section (3.3.2). Mass spectrometry measurements were performed during a number of depositions - of these, the silane depletion in the plasma is known.

Not all experiments gave rise to films suitable for quantification with EPMA. In the case of samples SP002 and SP003 (marked with an asterisk), the film on top of the upper substrate detached itself from the nickel substrate and ruptured after deposition. The upper substrates of depositions SP011, SP012, and SP014 (marked with a dagger) ripped, from the slit outward, after deposition. As these five depositions were all performed at higher temperatures, it is believed that this rupturing and ripping is due to different expansion coefficients of silicon and nickel ($4.68 \cdot 10^{-6}$ and $13.4 \cdot 10^{-6}$ K^{-1} respectively). As the (hot) substrates cool down, the nickel and the silicon contract at different speeds. If the silicon film is not bound very strongly to the nickel film, this will result in the silicon film letting go of the substrate and, as it is very thin, rupturing. If, on the other hand, the binding between the films is strong, the nickel substrate will rip. For this reason, depositions could not be performed at higher temperatures, to measure the surface reaction probability at temperatures above the

‡ The silane flow of 20 scc/s is an estimate. A silane flow of 10 scc/s was requested, but recalibration between depositions SP010 and SP011 indicated that the 'old' silane flows had been approximately twice that which was reported.

critical temperature at which hydrogen starts desorbing from the surface, according to the growth model.

3.6.2 EPMA Results of SP010

A number of substrates were examined with EPMA (see section 3.5). In all cases, the EPMA results consist of a depth profile along a scan perpendicular to the slit. The depth profiles for SP010 are shown in Figure 3.20, along with Lorentz-curve fits.

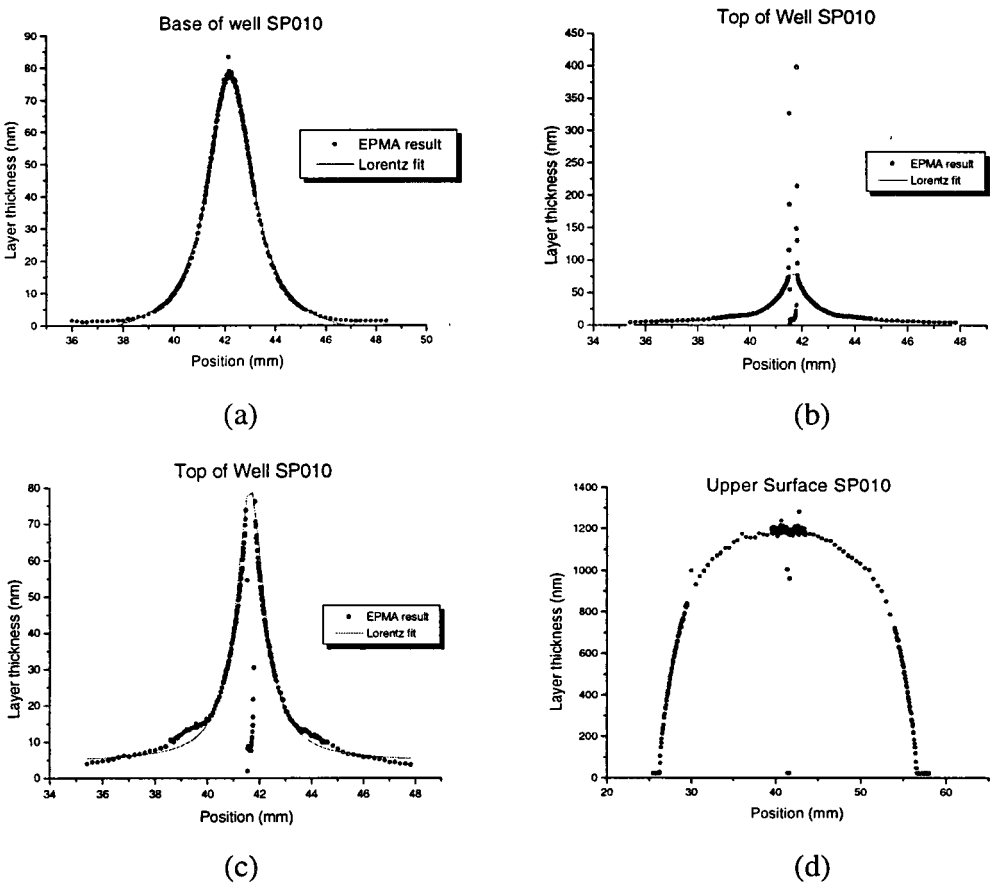

Figure 3.20: *Depth profiles of SP010, determined with EPMA.*

The EPMA results of the profiles of SP010 look physically acceptable. The profile of the base of the well can be closely approximated with a Lorentz curve, as shown in Figure 3.20 (a).

The profile of the top of the well appears to have a number of points, close to the slit, that are exorbitantly high. If these measurements are accurate they are difficult to explain physically, and there is no Lorentz or Gaussian curve that can approach this profile. However, it is quite likely that these points are a measurement error, as the sample was deformed by the heat of the plasma beam during deposition, particularly near the edges of the slit. This could have resulted in the detector being out of focus at

these points, see section 3.5.5. If these points are ignored, a Lorentz curve can be generated that fits the profile quite well, as shown in Figure 3.20 (c).

Finally, the profile of the upper surface of SP010 is homogeneous over a diameter of 1 cm. The substrate was covered by the ring that clamped it to the well at those points where the film thickness becomes zero. As previous measurements have shown that deposition is 90% homogeneous over a diameter of 8 cm. [VER95], it appears that the ring that clamps the well together from the top influences the homogeneity of deposition on top of the upper surface.

The goal of these measurements was to find the volume of deposition in the well. For this, the area of the Lorentz fits was taken as the area of the thickness profiles. To find the volumes T_{wb} and T_{wt}, this area was multiplied by the length of the slit (7.5 mm), as an approximation. The thickness t_s on top of the upper surface was simply found from Figure 3.20 (d), by taking the thickness at its maximum, at a few mm. from the slit.

3.6.3 EPMA Results of SP014

In contrast to the results for SP010, a number of samples had surprisingly irregular features. As an example, the EPMA results of SP014 are shown in Figure 3.21.

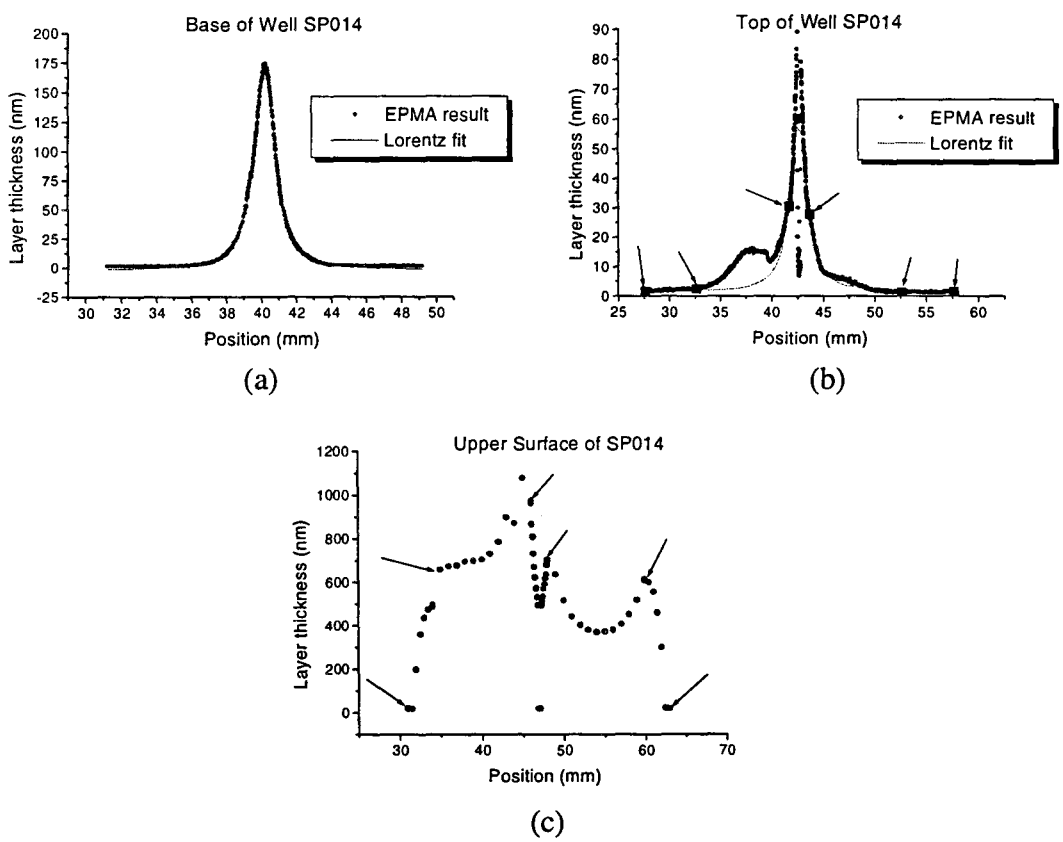

Figure 3.21: *Depth profiles of SP014, determined with EPMA.*

The profile for the bottom of the well looks, once again, very regular. The scans of both sides of the upper sample (with the slit) are, however, very unlikely. As the upper sample is not only much thinner than the lower, but also directly exposed to the plasma beam, it is deformed much more than the lower - this can easily be seen with the naked eye. Both sides of the upper sample were actually scanned in five individual scans, beginning and ending at the points marked with arrows. At each of these points, the detector was focused on the sample, so these are reliable. The scans themselves, however, are probably out of focus, as explained in section 3.5.6.

For the bottom of the well, a Lorentz curve was drawn through the six points at which the detector was focused. This eliminates the peculiar-looking bump on the left flank. As the height of the peak is unknown, this was varied until the Lorentz curve best fit the other six points. The area of the Lorentz curve was used in the determination of T_{wt}.

On the profile of the upper surface, even the points at which the detector was focused are probably not all correct. The outer four look acceptable, but the two nearest the slit differ too much to be realistic. The asymmetric appearance of the profile near the slit can be explained by symmetric distortion of the sample, and an error due to differences in absorption (see section 3.5.5). The upper surface is curved upward near the slit. If this deformation is symmetric around the slit, then the X-rays headed toward the silicon detector will have a path through the sample that is too short on one side of the slit, and too long on the other side, resulting in an asymmetric profile. This would mean that the true thickness near the slit lies between these two measured values - calculations were performed with t_s = 800 nm.

One question may come to mind: although SP014 ripped, SP010 looks just as badly deformed as SP014 to the naked eye, so why would SP014 yield such irregular profiles compared to SP010? The answer lies in the film thickness, which is much smaller in SP014, both in the well and on top of the upper surface. The result is a higher sensitivity to error; this problem could be solved by depositing thicker silicon films.

3.6.4 Additional sources of error:

In most cases, an additional error arises due to inaccuracy in the determination of the area under the Lorentz curve at the top of the well, and in determination of the film thickness on top of the upper sample, due to distortions in the sample. Additional sources of error are:

1. Deposition on the sides of the well, and
2. The simplification that $T_w = A_w \cdot L$, where A_w is the area of the profile and L is the length of the slit (see Appendix D).
3. The scan may not have been performed perfectly perpendicular to the length of the slit, resulting in a profile that is too wide.

All of these are neglected. Deposition on the sides of the slit is negligible compared to deposition elsewhere (see Figure 3.4), and deposition on the sides of the well can usually be avoided by working with a small well-height. Finally, using $T_w = A_w \cdot L$ appears to give a good approximation - see (Appendix D and Figure 3.10). T_w could

be determined more exactly if a scan were made parallel to the slit, but this is far more difficult than a scan perpendicular to the slit. The reason is that when the scan perpendicular to the slit is not completely perpendicular to the slit, this will result in a very small error. Programming a scan so that it is parallel to the slit is far more difficult, and will therefore result in a larger error.

As the density of silicon on the films being examined may very well differ from the density of crystalline silicon, this results in an error in the calculated thickness, as it is calculated by dividing the measured mass thickness by the density of crystalline silicon. However, the error in calculating the sticking probability and the surface reaction probability (see section 3.3.5), is negligible: as an erroneous density will result in a thickness t_s that is wrong by a certain factor, but also a volume in the well that is off by the same factor (doubling the height of the profile results in twice the volume), and as the formulas for β and s always involve relative thicknesses/volumes, the error will divide out.

In a number of cases (SP005, SP009, and SP017), the deposition at the top of the well turned out to be more than the deposition at the base of the well. This is impossible if both samples are at equal temperature, as any particles that stick to the bottom of the well have already reflected once. The only possible explanation is that the sticking probability at the top of the well is larger than the bottom of the well, in which case the approach described in section 3.3.6 is valid. However, this situation is unlikely to occur at the temperatures we used, which leaves this observation unexplained. It does not affect the determination of β if β is determined by comparing the total deposition in the well to the deposition on top of the upper surface.

Another source of error, which may not be neglected, is that of deposition on the sides of the slit. As the upper substrate's thickness is 50 μm, particles approaching the slit from certain angles cannot enter the slit but will react with the sides: the slit itself shadows the well, giving rise to a smaller effective slit area than the real slit area. This error is estimated in Appendix F.

3.6.5 Overall Results: Surface Reaction Probability and Growth Rate

The profiles measured with EPMA and the thicknesses on the upper surfaces were used to calculated the surface reaction probabilities of the depositions listed in Table 3.4. The method used is that of section 3.3.5 (assuming that the sticking probabilities are equal for both samples). Of the samples that ripped, an EPMA scan was made only of SP014. No scan was made of SP001 as this sample was sent to Marc Schaepkens in Albany for ellipsometry analysis. Furthermore, no scan was made of sample SP013, as deposition in the well extended all the way to the outside, so that there is probably deposition on the sides of the well, resulting in a large error when determining T_w. Growth rates were determined by dividing the film thickness on top of the upper surface by the deposition time.

Table 3.4: *Surface reaction probabilities and growth speeds of the slit experiments.*

Meas.	β	β_{corr}	β_{fract}	v_g (nm/s)	Yoke-temp. (°C)	Depletion (%)
SP001	??	??	??	??	150	
SP005	0.52 ± 0.07	0.5	1.10	10.0	30	
SP009	0.45 ± 0.04	0.4	1.06	9.6	100	
SP010	0.70 ± 0.07	0.6	0.563	40.0	130	
SP014	0.35 ± 0.06	0.3	0.450	4.4	200	22.7
SP015	0.7 ± 0.11	0.6	0.420	8.4	100	98.7
SP016	1.3 ± 0.3	1.1	0.512	1.7	100	45.2
SP017	1.30 ± 0.07	1.1	1.79	6.0	100	94.7

In the table, β indicates the value of the surface reaction probability when calculated by means of equation 3.17 (comparison of the material deposited in the well to what was deposited on the upper surface), β_{corr} is a rough indication of what β is equal to when corrections due to the shadowing effect of the sides of the slit are taken into account (see Appendix F), and β_{fract} is the outcome of the surface reaction probability when determined by means of equation 3.16 (comparison of the material deposited at the top of the well to that deposited at the bottom of the well). In further conclusions and discussion, the values of β_{corr} are used to compare the depositions.

The basic results (areas of profiles resulting in deposition volumes in the well, film thickness on top of the upper substrate, etc.) are listed in Appendix E.

3.7 Conclusions on Surface Reaction Probability

In order to compare the different surface reaction probabilities, the samples are first divided into two groups: variation of hydrogen flow and variation of substrate temperature.

3.7.1 Variation of Hydrogen Flow

Samples SP009, SP010, SP015, SP016, and SP017 were all deposited at the same yoke temperature, but with different SiH_4 and H_2 flows. Samples SP010 and SP015 (which were deposited with no hydrogen flow) both have surface reaction probabilities of approximately 0.6, which is close to the value of 0.7 that others have found for SiH_2. Sample SP009, on the other hand, was found to have a surface reaction probability of approximately 0.4. This is closer to the value of 0.37 that has been found for the SiH_3 radical by others. The values obtained from SP016 and SP017 are both larger than one, which is clearly impossible. This indicates that either the measurement was not performed correctly, or the model for the experiment is not correct. However, it does show that the surface reaction probability is high, which is still consistent with formation of the SiH_2 radical, or possibly the SiH or Si radicals. A safe conclusion is that an obvious difference is observed between the surface reaction probabilities of the samples deposited without or with very little hydrogen, and the sample deposited with a large hydrogen flow. The observations are consistent with

production of the SiH_3 radical when a large hydrogen flow is added, and production of SiH_x ($x < 3$) radicals when little or no hydrogen flow is added.

3.7.2 Variation of Temperature

Samples SP005, SP009, and SP014 were all deposited under similar flow conditions; that is, a silane flow of 10 or 20 scc/s and a hydrogen flow of 10 scc/s. These three depositions were, however, performed at three different yoke temperatures: 30, 100, and 200 °C respectively. It is unlikely that any of these samples (except possibly the top of the well in deposition SP014) exceeded the critical temperature of 350 °C, at which Matsuda measures an increase in the sticking probability (see Appendix C). Therefore, no sticking probabilities could be determined using the method described in section 3.3.6. The resulting surface reaction probabilities found are equal to 0.5, 0.4, and 0.3, in the same order. At this hydrogen flow, it is expected that SiH_3 is formed. However, the surface reaction probability in the case of deposition SP005, which is too high compared to the value of 0.37 found by others, could indicate that SiH_3 is not the only radical present, but that other radicals with a higher surface reaction probability may also be produced in relatively small amounts. According to the growth model as proposed by Matsuda et. al, β should be constant for temperatures beneath 500 °C. However, we find that it decreases with increasing temperature. Recent measurements of the growth rate versus the substrate temperature have backed this observation: the growth rate decreases as the temperature increases. According to the GPM growth model, a decrease in β with increasing temperature can only be explained by an increase in desorption of the SiH_3 radical (in its original form) off the surface after it has physisorbed (this is incorporated in r). The growth model, however, does not predict that this will occur, and therefore is not an accurate representation of our situation.

3.8 Summary

The surface reaction probability of particles formed in the plasma when no hydrogen was added, is close to the value which others have found for SiH_2. On the other hand, when large hydrogen flows are added, particles are formed that have a surface reaction probability that is closer to the value of SiH_3. This indicates that silane dissociation by means of argon ions leads to the formation of SiH_2, whereas silane dissociation by means of hydrogen leads to SiH_3.

4. Concluding Discussion

As discussed in section 2.5.3, the amount of hydrogen seeded into the arc has a large influence on the silane depletion. Similarly, the hydrogen flow has a great impact on the surface reaction probability (section 3.7.1). At zero hydrogen flow, the depletion is very high, and in this case silane is definitely dissociated by argon ions or metastables. Hydrogen formed in the dissociation of silane does not appear to influence these reactions, which suggests that the reactions take place close to the shock and that recirculating hydrogen cannot enter the plasma beam at that point. Theoretically, silane dissociation by means of ions results in SiH_2 as the main precursor. This is supported by surface reaction probability experiments performed under these same conditions (SP010 and SP015), which result in $\beta \approx 0.6$ - a value which is consistent with the value of 0.7 that other groups have found for the SiH_2 radical. The silane depletion measured during one of the surface reaction experiments under these conditions (SP015, depletion = 99%) conforms with the silane depletion measured under identical circumstances, in the depletion versus hydrogen flow experiment shown in Figure 2.9 (c): 99%. Depositions under these conditions had a high film growth rate, which could be due to a large radical flux, but is probably also due to the high sticking probability of the SiH_2 radical.

Formation of the SiH_2 radical could also occur by means of the reaction between silane and argon metastables - this would contribute to the silane depletion, but cannot be distinguished from silane dissociation by means of stable ions. No evidence is found of SiH_3 production, which could also result from silane dissociation by means of argon metastables; if SiH_3 is formed, it must have a low density compared to SiH_2. An increase in the arc current would, in this case, result in an even higher silane depletion (upto 100%) but most probably no change in the surface reaction probability, as the main precursor would still be SiH_2. An increase in the silane flow would probably result in a lower depletion, but again no change in the type of radical formed.

As shown in section 2.5.2, addition of a small hydrogen flow to the arc results in an immediate decrease in the depletion. This is taken to be due to quenching of the argon ions in the arc and the early expansion, as in reactions (2.12) to (2.14). Although hydrogen ions will be formed, these are also quenched rapidly and do not increase the silane depletion. While still on the left (decreasing) branch of the curve showing the silane depletion versus the hydrogen seed, addition of more hydrogen results in a further decrease in the depletion, indicating that ions are still present but in lesser quantities. Thus, it is still expected that the main precursor formed is SiH_2. Two surface reaction experiments were performed with small hydrogen flows: SP016 and SP017, at flows of 5 and 1 scc/s, and a silane flow of 2 scc/s. The depletions measured were 45.2 % and 94.7 %, which are consistent with the depletions at corresponding hydrogen flows in Figure 2.9 (c) (38% and 93%, respectively). Surface reaction probability experiments performed under these conditions both resulted in a surface

reaction probability of larger than one. This indicates that either the measurement or the model describing the deposition in the well is incorrect. It could also indicate formation of the Si and SiH radicals (which is not likely, considering the reactions that may occur). However, it does show that the surface reaction probability is high, which is consistent with formation of the SiH_2 radical. Comparison of the growth rates of these depositions and SP015 with their corresponding depletions shows that v_g increases strongly with increasing depletion, or with increasing equivalent flux (the amount of silane that was dissociated, that is, depletion times the silane flux). This, again, is consistent with the idea that the silane depletion is a measure for the flux of radicals to the substrate.

As the hydrogen flow is increased, the depletion reaches a minimum, after which it increases once again. This is consistent with a further quenching of ions, until silane is practically no longer dissociated by means of ions. However, silane depletion by means of atomic hydrogen increases as the hydrogen flow is increased - this is the explanation for the rise in the depletion for large hydrogen flows. Reaction with atomic hydrogen, however, is expected to yield the SiH_3 radical. Therefore, it would be expected that the main precursor at large hydrogen flows is SiH_3. Surface reaction probability experiments performed with a large hydrogen flow (SP005, SP009, and SP014) yielded surface reaction probabilities of approximately 0.5, 0.4, and 0.3, respectively. The silane depletion during deposition SP014 was 23%, which again conforms with the value found in Figure 2.9 (b), for the depletion at a hydrogen flow of 10 scc/s, just to the right of the minimum. Others (see section 3.2.1) have found that the surface reaction probability of the SiH_3 radical is approximately 0.37. Thus, the surface reaction probability of SP014 and SP009 approach that of SiH_3, and although that of SP005 is too high, there is a clear difference with the surface reaction probabilities found in the depositions with little or no hydrogen flow, suggesting that there is a difference in the dominant type of radical formed. In addition, comparison of SP005 and SP009 with SP010, which was deposited under zero hydrogen flow but otherwise similar conditions, shows a large difference in film growth rate. The growth rate of the films deposited with a large hydrogen flow is approximately one fourth of the growth rate of the film deposited without hydrogen flow. This is presumably due to a change in the radical flux, but could also in part be due to the differences in sticking probability of the SiH_2 and SiH_3 radicals.

The surface reaction probability was seen to decrease with increasing substrate temperature, by a factor of 1.7 between SP005 and SP014. In addition, the growth rate of the depositions also decreased, by about 1.1 (the growth rate of SP014 was multiplied by two to correct for the silane flow - this, however, makes comparison tricky). Nevertheless, this supports the decrease in surface reaction probabilities. Further proof of this observation is given by recent measurements of the growth rate as a function of the temperature - these also indicated a decrease in growth rate with increasing temperature.

As shown in section (2.5.4), disilane production appears to be dependent on the amount of silane present when the plasma is on. When silane is dissociated by ions, the depletion is high (see section 2.5.3), resulting in a high production of SiH_2 and little SiH_4. In that case, reaction (2.18) is limited by SiH_4, and addition of silane will result in more production of disilane. When a large hydrogen seed is added to the arc,

however, it is expected that SiH_3 is the main precursor, and the silane depletion is relatively low; i.e., little SiH_2 is formed and the dissociation of silane is low. Yet, silane still appears to be the limiting factor in the production of disilane. A possible explanation lies in the formation of disilane from two SiH_3 radicals. It is unlikely that this occurs in the gas-phase, but two SiH_3 radicals on the surface of the growing film can recombine to form Si_2H_6. In that case, addition of silane results in the production of more SiH_3, which in turn results in more disilane formation due to recombination.

All in all, the mass spectrometry and surface reaction probability experiment results are both consistent with the formation of the SiH_2 radical when little or no hydrogen is added to the arc, and the formation of the SiH_3 radical when large hydrogen flows are added. The expectation is that film deposition by means of the SiH_3 radical results in higher quality films, as is confirmed by the film qualities of previous depositions, as listed in section 3.1.

Suggestions for future measurements:

- In order to determine the exact conditions under which the various radicals are formed, and the influence of the plasma parameters on the production of these radicals, appearance potential mass spectrometry measurements on our plasma are suggested.
- The model describing deposition in the well should be revised. For example, the effect of a different sticking probability on top of the upper surface than at the top of the well (that is, on both sides of the upper substrate) should be considered.
- Slit experiments could be performed at higher temperatures, in order to gain insight into the development of the surface reaction probability with temperature. In addition, the method for determining the surface reaction probability that is valid when the top substrate temperature exceeds the critical temperature may be used in this case, so that s rather than β may be determined. However, this experiment would require stronger samples that don't rip after being exposed to high temperatures.
- Scans of the films produced in the surface reaction probability experiment could also be performed parallel to the slit, to determine the length of the profile and thereby the error made when multiplying a perpendicular area with the length of the slit.
- The Monte Carlo simulation program could be improved by adding γ, and including the possibility of particle interaction in the well. Also, it could be expanded to fit measurements, so that the angular distribution could be determined.

Works Cited

[BAL30] Balzers Quadstar 421, version 3.0, software documentation.

[BAS93] BASTIN, G. F., J. M. DIJKSTRA, H. J. M. HEIJLIGERS, and D. KLEPPER, "In-Depth Profiling with the Electron Probe Microanalyzer," *Microbeam Analysis* **2** (1993): 29-43.

[BER92] BERMAN, A., Vacuum Engineering Calculations, Formulas, and Solved Exercises, Academic Press, London, 1992.

[BRO96] BROEKSTEEG, M., Parameterstudie van Expanderend Thermisch Plasma gedeponeerd amorf gehydrogeneerd silicium, Traineeship report, Eindhoven University of Technology, department of physics, group: particle physics, subgroup: plama physics, 1996.

[DOU90] DOUGHTY, D. A., J. R. DOYLE, G. H. LIN, and A. GALLAGHER, "Surface Reaction Probability of Film-Producing Radicals in Silane Glow Discharges," *Journal of Applied Physics* **67** (10), (1990): 6220-6228.

[DUC86] DUCKWORTH, H. E., R. C. BARBER, and V.S. VENKATASUBRAMANIAN, Mass Spectroscopy, Cambridge UP, Cambridge, 1986.

[FRI] FRIEL, J. J., X-Ray and Image Analysis in Electron Microscopy.

[GAL88] GALLAGHER, A., "Neutral Radical Deposition from Silane Discharges," *Journal of Applied Physics* **63** (7), (1988): 2406-2413.

[GIE96] GIELEN, J. W. A. M., Plasma Beam Deposition of Amorphous Hydrogenated Carbon, PhD Thesis, Eindhoven University of Technology, department of physics, group: particle physics, subgroup: plasma physics, 1996.

[GRI93] GRIEKEN, R. E. VAN, and A. A. MARKOWICZ, ed., Handbook of X-Ray Spectrometry, Dekker, New York, 1993.

[GRI94] GRILL, A., Cold Plasma in Materials Fabrication: From Fundamentals to Applications, IEEE Press, New York, 1994.

[HAM94] HAMERS, E. A. G., Impurities in the ASTER System and Gas Composition of VHF Plasmas, Masters Thesis,Utrecht University, Debye Institute, 1994.

[HO89] HO, P., W. G. BREILAND, and R. J. BUSS, "Laser Studies of the Reactivity of SiH with the Surface of a Depositing Film," *Journal of Chemical Physics* **91** (4), (1989): 2627-2634.

[JEO] Invitation to the SEM World, For People who are Using the SEM for the First Time, booklet with the Jeol Superprobe JXA-8600SX EPMA.

[KAA97] Kaathoven, D. van, Traineeship report, to be published, Eindhoven University of Technology, department of physics, group: particle physics, subgroup: plama physics, 1997.

[KAE95] KAE-NUNE, P., J. PERRIN, J. GUILLON, and J. JOLLY, "Mass Spectrometry Detection of Radicals in SiH4-CH4-H2 Glow Discharge Plasmas," *Plasma Sources Schience and Technology* **4**, (1995): 250-259.

[KES96] KESSELS, E., The Influence of the Substrate Conditions on Plasma Beam Deposited a-C:H-films, Masters Thesis, Eindhoven University of Technology, department of physics, group: particle physics, subgroup: plasma physics, 1996.

[KUS87] KUSHNER, M. J., "On the Balance Between Silylene and Silyl Radicals in RF Glow Discharges in Silane: The Effect on Deposition Rates of a-Si:H," *Journal of Applied Physics* **62** (7), (1987): 2803.

[KUS88] KUSHNER, M. J., "A Model for the Discharge Kinetics and Plasma Chemistry during Plasma Enhanced Chemical Vapor Deposition of Amorphous Silicon," *Journal of Applied Physics* **63** (8), (1988): 2532.

[KUS92] KUSHNER, M. J., "Simulation of the Gas-Phase Processes in Remote-Plasma-Activated Chemical-Vapor Deposition of Silicon Dielectrics Using Rare Gas-Silane-Ammonia Mixtures," *Journal of Applied Physics* **71** (9), (1992): 4173.

[LIB94] LIEBERMAN, M. A., and A. J. LICHTENBERG, Principles of Plasma Discharges and Materials Processing, John Wiley and Sons, New York, 1994.

[MAT90] MATSUDA, A., K. NOMOTO, Y. TAKEUCHI, A. SUZUKI, A. YUUKI, and J. PERRIN, "Temperature Dependence of the Sticking and Loss Probabilities of Silyl Radicals on Hydrogenated Amorphous Silicon," *Surface Science* **227**, (1990): 50-56.

[MEU96] MEULENBROEKS, R., Molecular Processes in Expanding Plasmas: A Laser Spectroscopic Study, PhD Thesis, Eindhoven University of Technology, Department of physics, group: particle physics, subgroup: plasma physics, 1996.

[MOL95] MOLENBROEK, E. C., Deposition of Hydrogenated Amorphous Silicon with the Hot Wire Technique, PhD Thesis, University of Colorado, Department of Chamistry, 1995.

[MOR86] MORT, J., and F. JANSEN, Plasma Deposited Thin Films, CRC Press, Boca Raton, 1986.

[PER89] PERRIN, J., Y. TAKEDA, N. HIRANO, Y. TAKEUCHI, and A. MATSUDA, "Sticking and Recombination of the SiH3 Radical on Hydrogenated Amorphous Silicon: The Catalytic Effect of Diborane," *Surface Science* **210** (1989): 114-128.

[PER96] PERRIN, J., O. LEROY, and M. C. BORDAGE, "Cross-Sections, Rate Constants and Transport Coefficients in Silane Plasma Chemistry," *Contributions to Plasma Physics* **36** (1), (1996): 3.

[ROB83] ROBERTSON, R., D. HILLS, H. CHATHAM, and A. GALLAGHER, "Radical Species in Argon-Silane Discharges," *Applied Physics Letters* **43** (6), (1983): 544-546.

[ROB86a] ROBERTSON, R., and A. GALLAGHER, "Mono- and Disilicon Radicals in Silane and Silane-Argon DC Discharges," *Journal of Applied Physics* **59** (10), (1986):3402-3411.

[SAN95] SANDEN, M. C. M. VAN DE, R. J. SEVERENS, R. F. G. MEULENBROEKS, M. J. DE GRAAF, Z. QING, D. K. OTORBAEV, R. ENGELN, J. W. A. M. GIELEN, J. A. M. VAN DER MULLEN, D. C. SCHRAM, "The Role of Hydrogen During Plasma Beam Deposition of Amorphous Thin Films," *Surface and Coatings Technology* **74-75**, (1995): 1-9.

[SEV95a] SEVERENS, R. J., G. J. H. BRUSSAARD, H. J. M. VERHOEVEN, M. C. M. VAN DE SANDEN, and D. C. SCHRAM, "An Expanding Thermal Plasma for Deposition of a-Si:H," *Materials Research Society Symposium Proceedings* **377** (1995): 33-38.

[SEV95b] SEVERENS, R. J., G. J. H. BRUSSAARD, M. C. M. VAN DE SANDEN, and D. C. SCHRAM, "Characterization of Plasma Beam Deposited Amorphous Hydrogenated Silicon", *Applied Physics Letters* **67** (4), (1995): 491-493.

[SEV96] SEVERENS, R. J., M. C. M. VAN DE SANDEN, H. J. M. VERHOEVEN, J. BASTIAANSSEN, and D. C. SCHRAM, "On the Effect of Substrate Temperature on a-Si:H Deposition Using an Expanding Thermal Plasma," to be published in *Materials Research Society Symposium Proceedings* **420**, "Amorphous Silicon Technology," (1996)

[SHA88] SHAW, J. G., and C. C. TSAI, "Monte Carlo Simulations of Plasma-Deposited Amorphous Silicon", *Journal of Applied Physics* **64** (2), (1988): 699.

[SUU89] SUURMEIJER, E. P. Th. M., and J. VERHOEVEN, Vacuümtechniek, Nederlandse Vacuüm Vereniging, Meppel, 1989.

[VER95] VERHOEVEN, H.J.M., Electrical Characterization of Plasma Beam Deposited Amorphous Hydrogenated Silicon, Masters Thesis, Eindhoven University of Technology, department of physics, group: particle physics, subgroup: plasma physics (1995).

[WHI86] WHITE, F. A., and G. M. WOOD, Mass Spectrometry: Applications in Science and Engineering, Wiley, New York, 1986.

[YUN95] YUN, J-H. and S-K. PARK, "Theoretical Study of Step Coverage and Comparison with Experimental Results from Low Pressure Chemical Vapor Deposition Process of Tungsten Film," *Japanese Journal of Applied Physics* **34** (1995): 3216-3226.

[ZHA95] ZHANG, M., and Y. NAKAYAMA, "Radical Fluxes in Electron Cyclotron Resonance Plasma Chemical Vapor Deposition of Amorphous Silicon," *Japanese Journal of Applied Physics* **34** (1995): 5965-5970.

[ZHA96] ZHANG, M., and Y. NAKAYAMA, "Dominant SiH_x Radicals in Electron Cyclotron Resonance Plasma CVD," *Plasma Sources Science and Technology* **5** (1996): 260-264.

Appendix A:

Type of Flow in the Vacuum System

Whether the gas flow is molecular or viscous depends on the size of the Knudsen number K', which is greater than one for molecular flow. When the Knudsen number is smaller than 0.01, the gas flow is laminar, and between 0.01 and 1 it lies in the transition regime. The Knudsen number is defined as:

$$K' = \frac{\lambda}{d}, \tag{A1}$$

where λ is the mean free path of the molecules, and d the characteristic dimension of the vessel through which the gas flows. As an approximation, the mean free path of pure argon is given by ([SUU89] and [BER92]):

$$\lambda = \frac{kT}{\sqrt{2}\pi\,\delta_m^2 p}, \tag{A2}$$

where k is the Boltzmann constant, T is the absolute temperature in the pipe, p is the pressure in Pa, and δ_m is the molecular diameter of argon (in this case, atomic diameter):

$$\delta_m = (7.929 \cdot 10^{-25} b)^{1/3}. \tag{A3}$$

The van der Waals constant b is equal to 0.03219 L/mol, which equals $3.219 \cdot 10^{-5}$ m^3/mol for argon. This results in $\delta_m = 2.944 \cdot 10^{-10}$ m.

In the pipe leading from the reaction chamber to the mass spectrometer vessel, to the left (on the high-pressure side) of the pinhole, the gas temperature is approximately room temperature (295 K - this is an underestimation!) and the pressure is the same as that in the vessel during deposition, 20 Pa (0.2 mbar). Inserting those values into equation (A2) then results in a mean free path of $5.288 \cdot 10^{-4}$ m. To find the Knudsen number, λ is divided by the characteristic size of the pipe, which is about 2.5 cm. or 0.025 m. The outcome is $K' \geq 0.021$, meaning that the flow is in the transition between viscous and molecular.

In the pinhole, assuming that the pressure is still high, the mean free path is the same, and the characteristic length is the diameter of the pinhole: 100 µm. This results in $K' \geq 5.3$, which means the flow is molecular.

To the right of the pinhole, the temperature is the same but the pressure drops to $5 \cdot 10^{-5}$ Pa, resulting in a mean free path of 21.15 m. The characteristic length is once again equal to the pipe diameter, leading to $K' \geq 850$ - definitely molecular flow.

Appendix B:

Reaction Constants of the Chemical Reactions in the Plasma

B1. Silane Dissociation by Means of Ion Impact

Silane dissociation by means of argon or hydrogen ions primarily leads to SiH_3^+, which then becomes SiH_2:

$$Ar^+ + SiH_4 \xrightarrow{k_{1a}} SiH_3^+ + H + Ar$$

$$Ar^+ + SiH_4 \xrightarrow{k_{1b}} SiH_2^+ + H_2 + Ar$$

$$Ar^+ + SiH_4 \xrightarrow{k_{1c}} SiH^+ + H + H_2 + Ar$$

$$Ar^+ + SiH_4 \xrightarrow{k_{1d}} Si^+ + H_2 + H_2 + Ar$$

$$H^+ + SiH_4 \xrightarrow{k_2} SiH_3^+ + H_2$$

$$SiH_3^+ + e^- \xrightarrow{k_3} SiH_2$$

Reaction constant	Value (m^3/s)	Reference
k_{1a}	$2.4 \cdot 10^{-18}$	[KUS88]
	$8 \cdot 10^{-17}$	[KUS92]
	(12%) $1.7 \cdot 10^{-17}$	[PER96]*
	(78%) $3.9 \cdot 10^{-17}$	[PER96]†
k_{1b}	$1.66 \cdot 10^{-18}$	[KUS88]
	(8%) $1.7 \cdot 10^{-17}$	[PER96]
	(12%) $3.9 \cdot 10^{-17}$	[PER96]
k_{1c}	$4.20 \cdot 10^{-18}$	[KUS88]
	(21%) $1.7 \cdot 10^{-17}$	[PER96]
	(8%) $3.9 \cdot 10^{-17}$	[PER96]
k_{1d}	$1.18 \cdot 10^{-17}$	[KUS88]
	(59%) $1.7 \cdot 10^{-17}$	[PER96]
	(2%) $3.9 \cdot 10^{-17}$	[PER96]
k_2	$5 \cdot 10^{-16}$	[KUS88]
	$5 \cdot 10^{-15}$	[PER96]
k_3	?	

* Reference to Chatham. The percentage shows the branching ratio of the overall reaction between silane and argon ions.

† Reference to Fisher and Armentrout.

B2. Silane Dissociation by Means of Argon Metastables

Argon metastable dissociation of silane can yield:

$$Ar^* + SiH_4 \xrightarrow{k_4} SiH_3 + H + Ar$$

$$Ar^* + SiH_4 \xrightarrow{k_5} SiH_2 + H + H + Ar$$

$$Ar^* + SiH_4 \xrightarrow{k_6} SiH + H + H_2 + Ar$$

$$Ar^* + SiH_4 \xrightarrow{k_7} Si + 2H + H_2 + Ar$$

with reaction constants:

Reaction constant	Value (m^3/s)	Reference
k_4	$1.4 \cdot 10^{-16}$	[KUS88]
k_5	$2.6 \cdot 10^{-16}$	[KUS88]
	$4.6 \cdot 10^{-16}$	[KUS92]
k_6	$2.4 \cdot 10^{-17}$	[KUS92]
k_7	$1.8 \cdot 10^{-18}$	[KUS92]

B3. Quenching of Ions by Means of Hydrogen

Argon ions are quenched via reactions

$$Ar^+ + H_2 \xrightarrow{k_8} ArH^+ + H,$$

followed by:

$$ArH^+ + e^- \xrightarrow{k_9} Ar + H,$$

or the set:

$$ArH^+ + H_2 \xrightarrow{k_{10}} H_3^+ + Ar,$$

$$H_3^+ + Ar \xrightarrow{k_{11}} ArH^+ + H_2,$$

$$H_3^+ + SiH_4 \xrightarrow{k_{12}} SiH_3^+ + H_2 + H_2.$$

Hydrogen ions are quenched by means of charge exchange:

$$H^+ + H_2 \xrightarrow{k_{13}} H_2^+ + H.$$

Reaction constant	Value (m^3/s)	Reference
k_8	$7.4 \cdot 10^{-16}$	[KUS88]
k_9	?	
k_{10}	$1.5 \cdot 10^{-15}$	[KUS88]
k_{11}	$1 \cdot 10^{-17}$	[KUS88]
k_{12}	$5.16 \cdot 10^{-16}$	[KUS88]
k_{13}	?	

B4. Silane Dissociation by Means of Atomic Hydrogen

The reaction of silane with atomic hydrogen yields SiH_3.

$$H + SiH_4 \xrightarrow{k_{14}} SiH_3 + H_2.$$

Reaction constant	Value (m^3/s)	Reference
k_{14}	$2.7 \cdot 10^{-18}$	[KUS87]
	$2.8 \cdot 10^{-17} \exp(-1250/T)$	[PER96][‡]
	$2.5 \cdot 10^{-19}$	[PER96][§]

B5. Further Reactions of Radicals

SiH_3 can be dissociated to SiH_2:

$$H + SiH_3 \xrightarrow{k_{15}} SiH_2 + H_2, \text{ or}$$

$$SiH_3 + SiH_3 \xrightarrow{k_{16}} SiH_2 + SiH_4,$$

Reaction constant	Value (m^3/s)	Reference
k_{15}	$1 \cdot 10^{-16}$	[KUS88]
k_{16}	$3.9 \cdot 10^{-16}$	[PER96]

B6. Formation of Higher Silanes

Disilane is formed by means of the reactions:

$$SiH_2 + SiH_4 \xrightarrow{k_{17}} Si_2H_6^*,$$

$$Si_2H_6^* + SiH_4 \xrightarrow{k_{18}} Si_2H_6,$$

and trisilane by means of:

[‡] At high pressure.
[§] At 295 K.

$SiH_2 + Si_2H_6 \xrightarrow{k_{19}} Si_3H_8$

Reaction constant	Value (m^3/s)	Reference
k_{17}	$1 \cdot 10^{-17}$	[KUS88]
	$4.6 \cdot 10^{-16}$	[PER96]
k_{18}	$1 \cdot 10^{-16}$	[KUS88]
	$2 \cdot 10^{-16}$	[PER96]
k_{19}	?	

Appendix C:

Results of Temperature Measurements on the Surface Reaction Probability Setup

As described in section 3.3.2, the temperatures of the top (foil with slit) and base (foil without slit) of the well were measured while the setup was exposed to different kinds of plasmas, and under different initial conditions.

Heating and cooling of the samples:
Figure C1 shows the yoke temperature, the temperature of the base of the well, and the temperature of the top of the well, all as a function of time, while an argon plasma was directed at the top of the well. The yoke temperature is controlled - in this case it was set at 200 °C. The plasma was turned on when the base and the top of the well reached equilibrium temperatures of 190 °C and 179 °C, respectively.

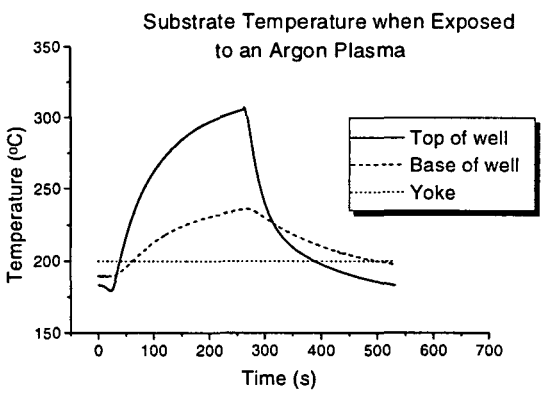

Figure C1: *Temperature increase due to an argon plasma.*

The temperature of the top of the well increased rapidly until it approached a maximum. After about 4.5 minutes, when it reached 306 °C, the plasma was turned off and the sample started cooling down. The temperature of the lower substrate followed the same trend, but warmed up considerably less, as it is not in direct contact with the plasma, and that it is influenced by the 'cold' yoke that it is mounted on. Note that both samples cooled off within a few minutes. This means that it is possible to let them cool down while still in vacuum, in order to avoid reactions between the hot surface and the air. Also, the samples cooled down to a temperature below that of the yoke, which suggests that they are capable of losing a lot of heat to the cold walls of the deposition vessel, by means of radiation.

Temperature increase versus initial yoke temperature:
The extent to which the plasma heats the samples depends on their initial temperature when the plasma is turned on. This initial temperature is always slightly lower than the yoke temperature, which is set. Figure C1 shows the final temperatures of the top

and base of the well, after exposure to the argon plasma. The samples' temperature increases less if they have a higher initial temperature.

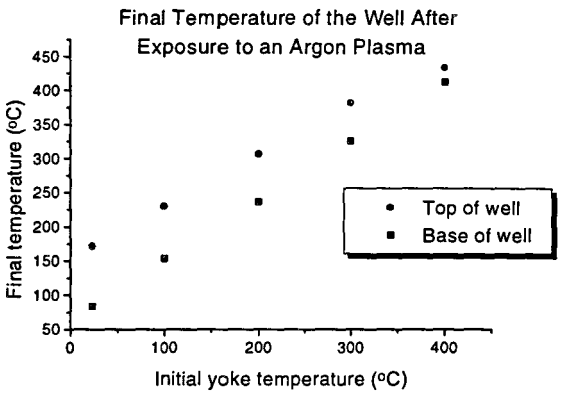

Figure C1: *Final temperature of the top and bottom of the well, due to an argon plasma.*

Temperature increase dependent on the type of plasma:
To determine the effect of a plasma with different gas compositions, the samples were exposed to the following plasmas, while the yoke temperature was constant at 300 °C:

1. Argon plasma (Argon flow 55 scc/s)
2. Argon/hydrogen plasma (flows respectively 55 and 10 scc/s)
3. Argon plasma (flow 55 scc/s) - reproducibility test
4. Argon/hydrogen/silane plasma (flows respectively 55, 10, and 10 scc/s) - deposition
5. Argon plasma (flow 55 scc/s) - reproducibility test.

The results are shown in Figure C2. Apparently, the argon plasma is most effective at heating the samples, and the temperature increase due to an argon/hydrogen plasma or an argon/hydrogen/silane plasma is considerably less. After the argon/hydrogen/silane plasma, the temperature increase due to an argon plasma was less, as the upper sample could lose more heat through radiation because of the roughness and dark color of the silicon deposition.

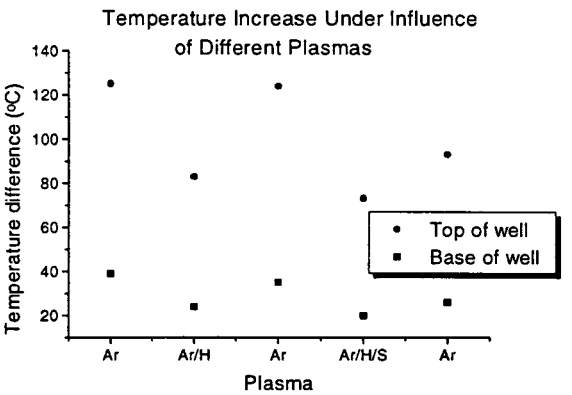

Figure C2: *Temperature increase due to different kinds of plasmas.*

Figure C1 and Figure C2 show that if a yoke temperature of 200 °C is used, and the samples are exposed to a deposition plasma, the final temperatures of the top of the well and the base of the well will be approximately 280 °C and 220 °C, respectively. These are both well below the critical temperature measured by Matsuda et. al., thus justifying the method of calculating the surface reaction probability described in section (3.3.5).

Appendix D:

Determination of the Volume in the Well

The volume in the well is determined by measuring the layer thickness profile of the a-Si:H layer perpendicular to the slit by means of EPMA, fitting a Lorentzian through the data points, integrating the curve to find the area, and multiplying by the slit length according to [DOU90]. In doing so, we ignore the deposited material at the back and front end of the slit (fig. D1). In this appendix an estimation is made of the amount of material deposited at those ends. This is done by using half of the Lorentzian that was determined for the profile, and rotating it around the far ends of the slit.

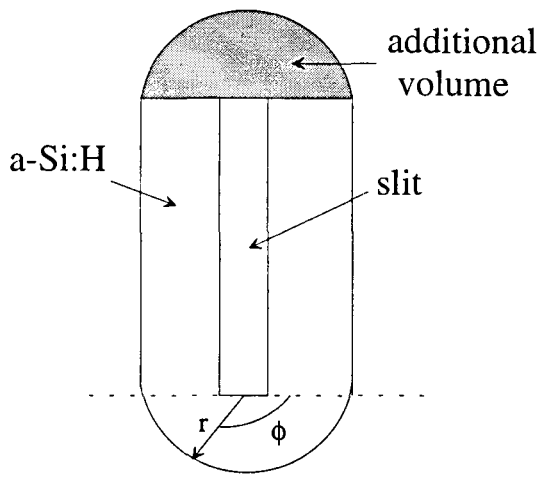

Figure D1: *Deposition at the ends of the slit.*

If we assume that the amount of deposited silicon only depends on the distance to the slit, and that the profile is Lorentzian, then:

$$H(z) = \frac{2Aw}{\pi}\frac{1}{4r^2 + w^2}, \tag{D1}$$

with:
$H(z)$ = height of the layer
A = area underneath the Lorentzian curve
w = half width at half maximum of the Lorentzian
r = distance to the slit

and the amount of material deposited at the front and back ends equals:

$$V = 2\int_0^{\pi}\int_0^{\infty}\frac{2Aw}{\pi}\frac{1}{4r^2 + w^2}\,r\,dr\,d\phi = 4Aw\int_0^{\infty}\frac{r}{4r^2 + w^2}\,dr = 4Aw\left[\frac{1}{8}\ln(4r^2 + w^2)\right]. \tag{D2}$$

As this integral is infinite we must restrict its borders. If we take the upper border to be twice the width of the Lorentzian curve ($2w$), the volume of the additional deposited material will be:

$$V = \frac{1}{2} Aw\left(\ln(16w^2 + w^2) - \ln w^2\right) = \frac{1}{2} Aw \ln 17. \qquad \text{(D3)}$$

For typical values of A en w (A=275 mm×nm and w=2.11 mm, SP010) this results in V=822 mm^2×nm. Compared to the estimation used in this thesis, $V=A\times L$=2063 mm^2×nm, this is an additional 28%.

However, as can be seen with naked eye and is also shown in the Monte Carlo simulations (Figure 3.12), the amount of deposited material decreases toward the end of the slit. Therefore, 'sticking' the Lorentzian to the far edge of the slit (lengthwise) and then rotating yields an overestimation of the volume at the ends, as the layer thickness declines *before* the edge of the slit. The exact position at which the Lorentzian *should* be stuck to are unknown, but could be determined by means of an EPMA scan parallel to the slit. However, from the Monte Carlo simulation it appears reasonable to estimate the amount of deposited material by $V=A\times L$.

Appendix E:

Results of Surface Probability Experiments

Conditions under which the surface reaction probability depositions were performed:

Meas.	Remarks	Well-height (mm)	H_2-flow (scc/s)	SiH_4-flow (scc/s)	Yoke-temp (°C)	Depo-time (min)	Analysis	Depletion (%)
SP001	OK	3.3	10	10	150	1		
SP002	ruptured	3.3	10	10	320	3		
SP003	ruptured	1	10	10	310	2		
SP004	on c:Si	--	10	10	320	3		
SP005	OK	0.5	10	10	30	3	SEM	
SP006	Carbon	1	--	--	60	0.5		
SP007	Carbon	1	--	--	60	1.75		
SP008	Thermo	2	var	var	var	var		
SP009	OK	1	10	10	100	3	SEM	
SP010	OK	1	0	10	130	0.5	SEM	
SP011	ripped	1	10	10	200	2		
SP012	ripped	1	10	10	200	2		
SP013	OK	1	10	10	200	3		22.6
SP014	ripped	0.5	10	10	200	3	SEM	22.7
SP015	OK	0.5	0	2	100	1.5	SEM	98.7
SP016	OK	0.5	5	2	100	2	SEM	45.2
SP017	OK	0.5	1	2	100	4		94.7

EPMA results, with the areas of the profiles determined by means of Lorentz fits.

Meas.	A_{wb} (m^2)	A_{wt} (m^2)	t_s (nm)	v_g (nm/s)	$T_{wb} = A_b * L$ (m^3)	$T_{wt} = A_d * L$ (m^3)
SP005	$410 \cdot 10^{-12}$	$450 \cdot 10^{-12}$	1800	10.0	$3.075 \cdot 10^{-12}$	$3.375 \cdot 10^{-12}$
SP009	470 "	500 "	1730	9.6	3.525 "	3.75 "
SP010	275 "	155 "	1200	40.0	2.063 "	1.163 "
SP014	400 "	180 "	800	4.4	3.000 "	1.35 "
SP015	189 "	80 "	760	8.4	1.418 "	$6 \cdot 10^{-13}$
SP016	25.6 "	13.1 "	207	1.7	$1.920 \cdot 10^{-13}$	$9.83 \cdot 10^{-14}$
SP017	97 "	174 "	1440	6.0	$7.275 \cdot 10^{-13}$	$1.305 \cdot 10^{-12}$

Appendix F:

Error Due to Shadowing of the Well, Due to the Thickness of the Upper Substrate

Particles entering the slit with a certain incoming angle ϕ can collide with the sides of the slit. If they then react with the surface, they are unable to enter the well. This gives rise to a measured value of T_w that is too low, due to deposition on the sides of the slit; this effect can be described as an *effective* slit area A_s' that is smaller than the actual slit area A_s. The situation is depicted in Figure F1:

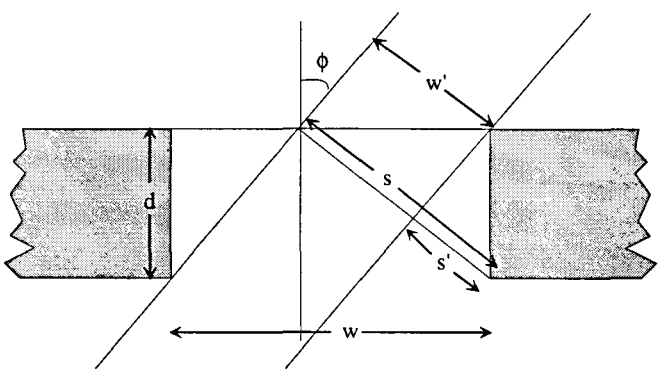

Figure F1: *Shadowing of the well due to the slit depth.*

The width of the slit as seen by a particle coming in at an angle ϕ to the vertical is s. Part of this is shadowed by the side of the slit: s'. The actual width of the slit is defined as w, and the thickness of the substrate is d. The idea is to calculate the effective width of the slit w', as seen by an incoming particle. The quantities s and s' are given by:

$$\left.\begin{aligned} s &= w\cos\phi \\ s' &= d\sin\phi \end{aligned}\right\}, \tag{F1}$$

so that from Figure F1 the effective width of the slit is equal to:

$$w' = \int_{\phi=0}^{\phi=\arctan(w/d)} (w\cos\phi - \beta d\sin\phi)d\phi\,, \tag{F2}$$

which can be solved to give

$$w' = w\sin[\arctan(w/d)] + \beta d\cos[\arctan(w/d)] - \beta d\,. \tag{F3}$$

Then, from Figure F1, the arc tangents can be substituted:

$$w' = \frac{w^2}{\sqrt{w^2 + d^2}} + \frac{\beta d^2}{\sqrt{w^2 + d^2}} - \beta d = \frac{w^2 + \beta d^2}{\sqrt{w^2 + d^2}} - \beta d. \tag{F4}$$

Obviously, the magnitude of the correction depends on the size of β. In the limit for very small β, w' becomes equal to:

$$w' = \frac{w^2}{\sqrt{w^2 + d^2}} = w\cos\phi = s, \tag{F5}$$

which is equal to the actual width of the slit seen under an angle, so that the correction is negligible. If, on the other hand, β approaches one, then

$$w' = \frac{w^2 + d^2}{\sqrt{w^2 + d^2}} - d = \sqrt{w^2 + d^2} - d. \tag{F6}$$

Inserting the actual width of the slit w = 250 μm and the thickness d = 50 μm then yields:

$$w' = \sqrt{1.04}w - 0.2w \approx 0.8w.$$

Thus, the correction is 20% when β is equal to one, and negligible when β approaches zero.

Appendix G:

The Monte Carlo Simulation Program Flowchart

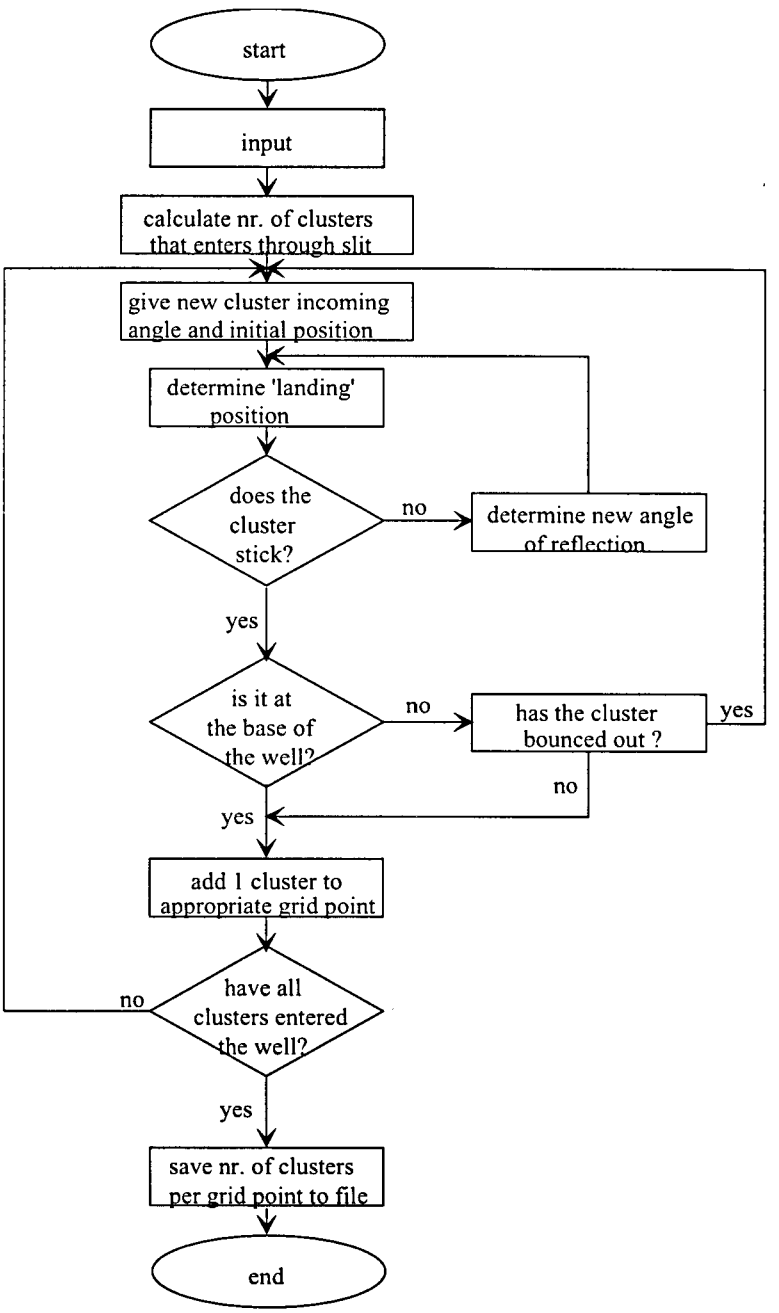

Appendix H:

Deuterated Silane

What is the cause of the peak at *m/z* = 34?

1. $^{30}SiH_3D$? This is a possibility, as its fragmentation ion $^{30}SiH_2D^+$ would generate a peak at *m/z* = 34.
2. $^{29}SiH_2D_2$? This is *not* possible: apart from the peak at *m/z* = 34 due to $^{29}SiHD_2^+$, we would have to see a peak at *m/z* = 35 due to $^{30}SiHD_2^+$ in accordance with the silicon isotope ratio, i.e. ^{29}Si : ^{30}Si= 4.7 : 3.1 = 1.5 : 1. However, *no* signal is observed at *m/z* = 35.
3. $^{28}SiHD_3$ or $^{28}SiD_4$? Possible, but unlikely. Both would give a peak at *m/z* = 34 due to $^{28}SiD_3^+$ and an undetectably small peak at *m/z* = 35 (92.2 : 4.7), but it seems unreasonable to assume the density of $SiHD_3$ and SiD_4 is higher than that of SiH_2D_2.

So if *m/z* = 34 is due to SiH_3D, how much of that is there in our plasma?

Approximately 4% of the SiH_4 quantity. The *m/z* = 34 signal due to $^{30}SiH_2D^+$ is 2.2×10^{-12} A (at the condition $Ar/D_2/SiH_4$ = 55/8/10 and 45A current). Given the isotope ratio of ^{28}Si : ^{30}Si = 92.2 : 3.1, we would have to have a contribution of $(92.2/3.1)\times2.2\times10^{-12} = 6.5\times10^{-11}$ A at *m/z* = 32 due to $^{28}SiH_2D^+$. If we now suppose that the current at *m/z* = 31, i.e. 1.66×10^{-9} A, is mainly due to $^{28}SiH_3^+$ (that is, we assume that the fraction of D-containing radicals is small), it follows that:

$$\frac{SiH_3D}{SiH_4} = \frac{6.5\times10^{-11}}{1.66\times10^{-9}} = 0.04$$

Is 4% of SiH_3D in SiH_4 consistent with the observed behavior of *m/z* = 33?

Yes it is. Based on the change of the currents at *m/z* = 28 to 31, we conclude that the depletion of SiH_4 is approximately 10%. If there were no SiH_3D, the signal at *m/z* = 33 (in that situation exclusively due to $^{30}SiH_3^+$) would also have to decrease by 10%, which is 5.3×10^{-12} A. However, we will now show that the contribution due to fragmentation of 4% SiH_3D cancels out this decrease for *m/z* = 33, consistent with the observation that at this exact plasma setting, the *m/z* = 33 signal does *not* change.

For SiH_4, the fragmentation library gives 0.07 : 0.02 = 3.5 : 1 for the branching ratio of *m/z* = 32 (due to $^{29}SiH_3^+$ and $^{30}SiH_2^+$) to that of *m/z* = 33 (due to $^{30}SiH_3^+$), and using the isotope ratio of ^{29}Si : ^{30}Si = 1.5 : 1, we find the following branching ratio: $^{30}SiH_2^+$: $^{29}SiH_3^+$: $^{30}SiH_3^+$ = 2 : 1.5 : 1. Similarly, we find that the ratio between $^{29}SiH_2D^+$ and $^{30}SiH_2D^+$ is also 1.5 : 1, for the branching of SiH_3D. For the ratio $^{30}SiHD^+$ to $^{30}SiH_2D^+$ however, we can use the same ratio as $^{30}SiH_2^+$ to $^{30}SiH_3^+$ (2:1), but we must correct for the fact that 1/3 of the reactions leads to $^{30}SiH_2^+$ and only 2/3 to $^{30}SiHD^+$:

$^{30}SiHD^+$: $^{29}SiH_2D^+$: $^{30}SiH_2D^+$ = 1.3 : 1.5 : 1.

The two leftmost terms are the deuterium-related contributions to m/z = 33, whereas $^{30}SiH_2D^+$ corresponds to the m/z = 34 signal. In effect, this means that the deuterium-related increase of the m/z = 33 signal is 2.8 times larger than the m/z = 34 signal, or $2.8\times 2.2\times10^{-12} = 6.1\times10^{-12}$ A, which is 12% of the actual signal.

In other words: The change of the m/z = 33 signal is -10% (due to depletion) + 12% (due to a contribution of SiH_3D with an abundancy of 4%) = +2%. Given the rough nature of this calculation, this corresponds very well with the observation.

Acknowledgements

First and foremost, a word of thanks is in order for René Severens, who supervised me during the past year: thanks for your patience and time, and I'm looking forward to seeing those chapters in your thesis! I enjoyed the time we spent working together very much, and this includes all the good times after work. Besides René, I am also indebted to my other supervisors Richard van de Sanden and Daan Schram, for their guidance and for making sure I never ran low on work and ideas. For help with computer problems and optics, I would like to thank Bertus Hüsken (I'm sorry for having tested your patience so often!) and Herman de Jong. Ries (Stroei....) van de Sande proved to be invaluable for technical assistance. I admire his ingenuity, and advise him to keep on singing, as it may start sounding good eventually! I promised Ries that he would appear in my thesis with a star, so here it is: ☆! It has been said that I have a knack for setting Bertus and Ries to work for me, but I would like to counter this: it was not my pushing or extraordinary (female) talents that always got them working for me, but their own enthusiasm!

I am very much indebted to a number of people at the chemistry department for enabling me to perform the EPMA measurements. One of these is Giel Bastin, whom I would like to thank for allowing me to use the TFA program. However, special thanks go out to Pascal Oberndorf and particularly Hans Heijligers who spent many, many hours helping me perform the measurements; this thesis would have been half as thick if it had not been for their help. Whenever I had new samples, all I had to do was make a phone call and Hans was ready to set up a measurement for me - especially towards the end when I was in a big hurry. I enjoyed working with you and hope the Voyager problems really *were* due to my presence, and that they are solved now that I am no longer around the machine!

I would like to thank the rest of the group (AIO's and students) for the nice time during lunch and coffee breaks. A special thanks goes out to the 'Thursday evening' group (you know who you are, but I'll try to list most of you) for making life after work bearable: Seth Brussaard, Ariël de Graaf, Frank de Groote, Ger Janssen, Jeroen Jonkers, Erwin Kessels, Karine Letourneur, Roger Paffen, René Severens, Guiseppina (Pina) Toto, and Eric Verhoeven. I hope we can continue this good habit. To encourage you, let me remind you that I now have a salary and intend to make up for not quite having payed my share of rounds for a while!

Finally, I'd like to thank my parents, my sister Barbra + $Eric_2$, and Eric for their support and unfaltering belief in me. Thanks!